Faculty of Mechanical Engineering

THERMAL RECTIFICATION AT SOLID-LIQUID INTERFACE OF SIMPLE LIQUID IN CONTACT WITH FACE CENTERED CUBIC LATTICE

Nikki Han Tin Loon

Bachelor of Mechanical Engineering

2018

THERMAL RECTIFICATION AT SOLID-LIQUID INTERFACE OF SIMPLE LIQUID IN CONTACT WITH FACE CENTERED CUBIC LATTICE

NIKKI HAN TIN LOON

UNIVERSITI TEKNIKAL MALAYSIA MELAKA

THERMAL RECTIFICATION AT SOLID LIQUID INTERFACE OF SIMPLE LIQUID IN CONTACT WITH FACE CENTERED CUBIC LATTICE

NIKKI HAN TIN LOON

A thesis submitted
in fulfilment of the requirements for the Degree of
Mechanical Engineering

Faculty of Mechanical Engineering

UNIVERSITI TEKNIKAL MALAYSIA MELAKA

2018

DECLARATION

I declare that this project entitled "Thermal rectification at solid-liquid interfaces of simple liquid in contact with face-centered cubic lattice" is the results of my own excepts as cited in references.

Signature : ………..……………………

Name : Nikki Han Tin Loon

Date : 16/01/2019

APPROVAL

I hereby declare that I have read this project report and in my opinion this report is sufficient in terms of scope and quality for the award of the degree of Bachelor of Mechanical Engineering (BMCG).

Signature : ……………..............................

Supervisor Name : …………………………………

Date : …………………………………

ABSTRACT

A molecular dynamic study on the influences of the surface structure of solid on the thermal rectification at solid-liquid (S-L) interfaces of three types of face-centered cubic lattices namely are (100), (110) and (111) in contact with a simple liquid. Thermal rectification (TR) is defined as the differences in thermal energy transfer for two opposite directions of heat flow from the solid to the liquid and vice versa. In this project, the TR is evaluated based on the thermal boundary conductance TBC at the S-L of the two opposite directions of heat flow. The differences of the TBC between the two opposite directions of heat flow will be reported.

ABSTRAK

Satu kajian dinamik molekul mengenai pengaruh struktur permukaan pepejal keatas pembetulan haba pada antara muka pepejal-cecair (S-L) dengan tiga jenis kekisi berpusat muka padu kubik iaitu (100), (110) dan (111) bersentuhan dengan cecair mudah. Pembetulan termal (TR) ditakrifkan sebagai perbezaan aliran haba dari pepejal ke cecair dan sebaliknya. Dalam projek ini, TR akan dinilai berdasarkan kekonduksian sempadan termal (TBC) pada antaramuka S-L dari dua arah bertentangan aliran haba. Perbezaan TBC antara kedua-dua arah bertentangan aliran haba akan dilaporkan.

ACKNOWLEDGEMENT

First of all, I praise to almighty god for having made everything possible by giving me the strength and courage to complete this Final Year Project. I also would like to take this opportunity to express my profound gratitude and deep regards to my supervisor Dr Abdul Rafeq bin Saleman for his vital encouragement, monitoring and guidance throughout this project. Furthermore, I would like to thanks my parents, and friends for their constant encouragement without which this project would not be possible. Last but not least, I would like to express my deepest appreciation to all those who provided me the possibility to complete this project.

TABLE OF CONTENTS

PAGE

CHAPTER

1. INTRODUCTION

2. LITERATURE REVIEW

3. METHODOLOGY

4. RESULT AND DISCUSSION

5. CONCLUSION

LIST OF TABLES

LIST OF FIGURES

LIST OF APPENDICES

LIST OF ABBRREVIATIONS

S-L	Solid-Liquid
S-S	Solid-Solid
FCC	Face Centered Cubic
TBR	Thermal Boundary Resistance
TR	Thermal Rectification
PBC	Periodic Boundary Condition
NVE	Constant Particle Number (N), Volume (V) & ∑ Energy (KE & PE)
NVT	Constant Particle Number (N), Volume (V) & Temperature (T)
NPT	Constant Particle Number (N), Pressure (P) & Temperature (T)
CPU	Center Processing Unit
AMM	Acoustic Mismatch Model
DMM	Diffuse Mismatch Model
TraPPE	Transferable Potential for Phase Equilibria
TBR	Thermal Boundary Resistance
TBC	Thermal Boundary Conductance
TRR	Thermal Rectification Ratio

LIST OF SYMBOLS

τ_p	Barostat Relaxation Time Step
$\dot{A}$	Angstrom
Φ	Interaction Energy
α	Width Control Potential
$-e$	Electron Charge
$\emptyset$	Electrostatic Potential
Z	Acoustic Impedance
ρ	Density
c	Speed of Sound
$\mathbf{F}_s$	Short Range Force
$\mathbf{F}_l$	Long Range Force
E_F	Electrochemical Potential
J_S	Control Surface Heat Flux

CHAPTER I

INTRODUCTION

1.1 Background of study

Thermal rectification (TR) is a phenomenon where heat is easily flow in one direction but much harder to flow in the opposite direction between two materials. In other words, TR can also be defined as the differences in thermal energy transfer between two opposite directions of heat flow between two materials in contact with each other. The two materials in contact with each other can either be the contact between solid to solid or solid to liquid, where the contact interfaces are referred here as solid-solid (S-S) interfaces and solid-liquid (S-L) interfaces, respectively.

The phenomenon of thermal rectification was first discovered by Starr in early of 1935 during an experimental investigation of the contact between copper and cuprous oxide, where it showed thermal as well as electrical rectification. However, during that time, thermal rectification did not gets much attentions from researchers. In the year of 2002, thermal rectification was reintroduced by Terraneo et al. by utilizing a nonlinear one-dimensional chain of molecules between two thermostats at various temperatures. In the year of 2004, Li et.al conduct a similar study as the Terraneo at which Li et.al used two non-linear segments coupled together by a constant harmonic spring which use the Frenkel-Kontorova (FK) model (B.Li, 2004). In recent years, due to the development of nanotechnologies attracted considerable attention from researchers in various field to investigate thermal rectification since it can be utilized in a number of engineering applications such as thermal diode and thermal transistor (S. Pristic, 2010)

In the past, most of the investigation on the thermal rectification was done towards the S-S interfaces. As such, the studies on thermal rectification towards the S-L interfaces is less numerous. The thermal rectification at S-L interfaces as first done by Hu et al, that stated the thermal rectification of S-L interface are influence by modified the surface. Next, Murad et.al stated the thermal rectification at S-L interface relies greatly on the interfacial thermal resistance and mass density (S.Murad, 2014) (S. Murad, 2012). As for this research, the S-L interface is more priority compare to S-S as the liquid are easy to manipulate unlike solid which fix to its lattices and are hard to manipulate.

Although there are a number of studies on the thermal rectification in the past, the studies related to thermal rectification at S-L interfaces is still less numerous. As such this project would like to investigate the thermal rectification at S-L interfaces.

In the past studies of thermal rectification at S-L interfaces, the behaviour of the thermal rectification was measured based on the interfacial thermal resistance at the S-L interfaces, which is also known as Kapitza resistance, thermal boundary resistance (TBR) or thermal boundary conductance (TBC). Here, the inverse of TBR is the TBC. The interfacial thermal resistance at the S-L interfaces is defined as the measurement of resistance to the thermal energy transfer at the contacting surfaces of solid and liquid that results in temperature discontinuity at the contacting surfaces (E.T Swartz, 1989) (T. Ohara D. , 2010). Molecular dynamics (MD) simulation have revealed that the interfacial thermal resistance at the S-L interfaces was influenced by the molecular interaction between solid and liquid molecules (A. Amania, 2016) (B.H. Kim, 2008) (T.Q V. B., 2015) (M. Barisik, 2012), surface morphology (T.Q V. B., Interface thermal resistance between liquid water and various metallic surfaces, 2015) (T.Q V. B., Transport phenomena of water in molecular fludic channels, 2016) and the influences of the atomic-scale structure of solid (T. Ohara D. , 2005) (D. Toruu, 2010) (Abdul Rafeq bin Saleman).

1.2 Problem Statement

In the past, thermal rectification was investigated based on the modified surface of solid, applied external forces and influences of molecular interaction between solid and liquid. Even though in the past studies have revealed that molecular scale structure of solid surfaces influences the thermal energy transfer across solid-liquid (S-L) interfaces, the influences of molecular scale structure of solid surfaces on thermal rectification have yet to be determine. As such, this study will be focusing on the thermal rectification at the S-L interfaces between simple liquid and solid surface with the structure of face-centered cubic (FCC). The influences of the surface structure of solid surfaces on the thermal rectification will be measured based on thermal boundary conductance (TBC) at the solid-liquid interfaces. The thermal boundary conductance (TBC) at the S-L interfaces will be measure for two opposite heat flow directions across the interfaces. The thermal energy transfer across the S-L interfaces will be investigated using non-equilibrium molecular dynamics (NEMD) simulations and finally the influences of surface structure of solid on the thermal rectification will be clarify.

1.3 Objective

The aim of this research is:

I. To identify the influence of thermal rectification effects at solid-liquid (S-L) interface of a simple liquid and face-centered cubic (FCC) lattice.

II. To identify the influence of surface structure of solid on the thermal rectification at S-L interfaces.

1.4 Scope

The scopes are identified based on the objectives of this project. The simulation model which is consisted of the liquid confined between two parallel solid walls will be developed. Three type of surface structure of the face-centered cubic (FCC) lattice will be utilized, namely are (100), (110) and (111) crystal planes. In this study the simple liquid consists of a liquid with simple molecules will be utilized. A constant value and amount of heat flux with two directions of heat flows will be applied on the simulation model, one from solid to liquid and vice versa. The interfacial thermal resistance at the S-L interfaces will be evaluated by using thermal boundary conductance (TBC). The evaluation of the TBC and the related parameters needed for the evaluation will be shown later. This study will be focusing on the influences of the surface structure of the solid walls on the characteristics of TBC.

1.5 Significant of Study

The significant of this study is to identify the influences of thermal rectification at S-L interface of a simple liquid with three type of FCC by measuring the TBC at the interfaces. In addition, this study will identify the influence of surface structure of solid on the thermal rectification at S-L interfaces. The finding will clarify the characteristics of the interfacial thermal resistance at the S-L interface. The application of thermal rectification not only brings benefit to the individual but for society such as the use of lubricant in the engine to encounter the heat in the car engine and coating on the jet engine turbine to protect the blade at the high operating temperature.

1.6 Flow Chart

Figure 1.1 below show the flow chart of the final year project:

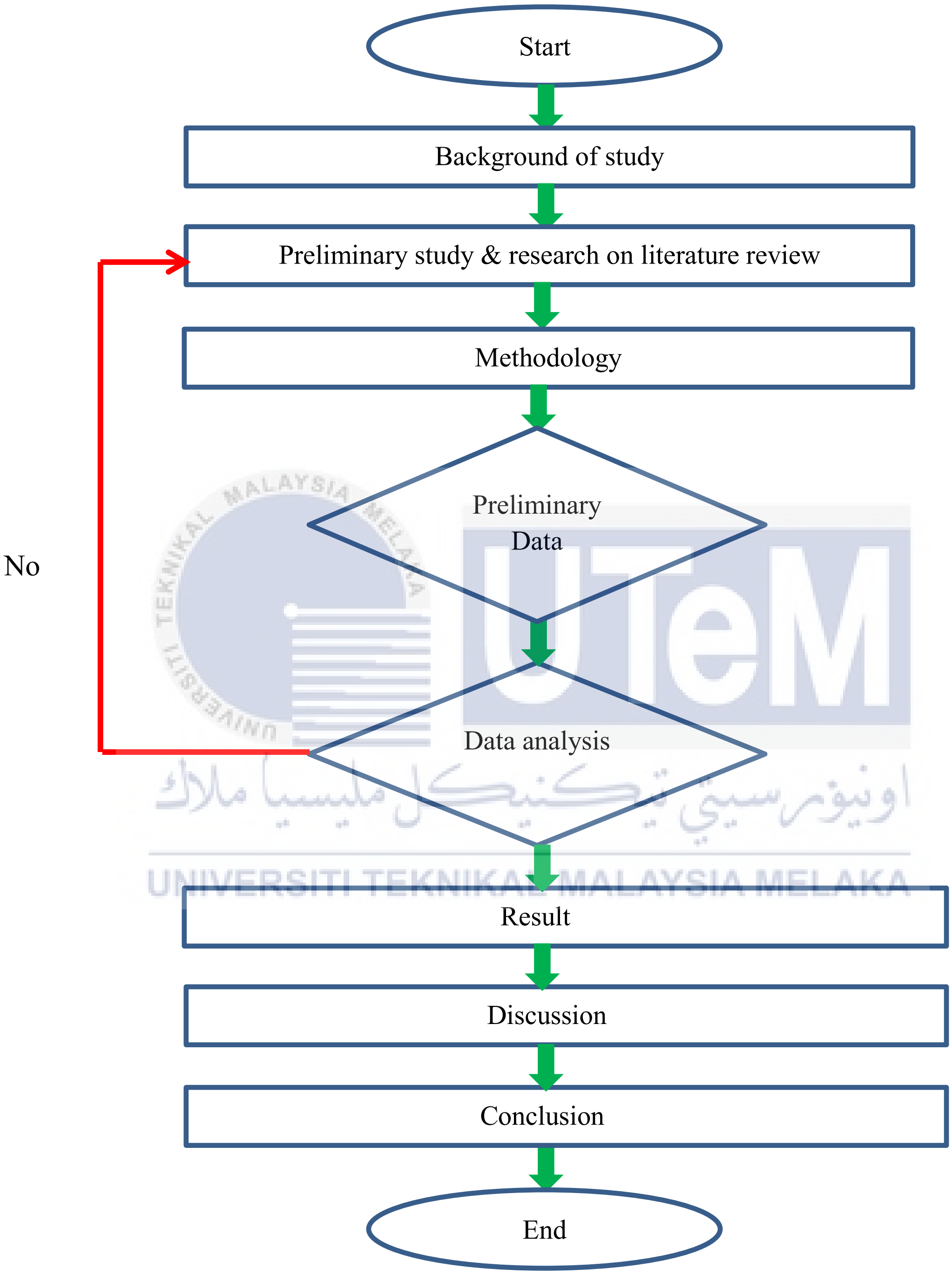

Figure 1.1 Flow chart

1.7 Flow Chart Explanation

1. Journals, article or any source of materials regarding to the project will be studied. Planning about the PSM 1 and 2 is done by constructing Gantt chart after a few discussions with lecturer.
2. The theory and research of thermal rectification at solid-solid interface and solid-liquid interface is studied for better understanding in direction and influence of heat flow.
3. After study on the previous thesis regarding about the thermal rectification of solid-liquid interface of this project. The information about the methodology of this project is obtained.
4. Verification of thermal rectification at solid-liquid interface is verified by using molecular dynamic simulation.
5. The result in this project is being analysed. The influence of thermal rectification effects at solid-liquid (S-L) interface of a simple liquid at face-centered cubic (FCC) and the influence of surface structure of solid on the thermal rectification at S-L interfaces is discussed.
6. For conclusion, a further study on thermal rectification at solid-liquid interface is described.
7. A report on this study will be written at the end of this project.

1.8 Gantt Chart

Final Year Project I (Gantt Chart)

No	Activity	Planning / Week	1	2	3	4	5	6	7	8	9	10	11	12	13	14	15	16
1	Briefing on Topic	Plan	🟦							🟨								🟨
		Actual	🟩							🟨 M								🟨
2	Background of Study	Plan		🟦	🟦					🟨 I								🟨 S
		Actual		🟩	🟩					🟨 D								🟨 T
3	Completed Chapter 1: Introduction	Plan			🟦					🟨								🟨 U
		Actual			🟥	🟩				🟨 S								🟨 D
4	Preliminary Study & Research on Literature Review	Plan			🟦	🟦	🟦	🟦	🟦	🟦 E	🟦	🟦	🟦	🟦	🟦	🟦	🟦	🟦 Y
		Actual			🟩	🟩	🟩	🟩	🟩	🟩 M	🟩							🟨
5	Discuss on Literature Review	Plan			🟦	🟦	🟦	🟦	🟦	🟦 E	🟦							🟨
		Actual			🟩	🟩	🟩	🟩	🟩	🟩 S	🟩							🟨
6	Chapter 2: Literature Review (Draft)	Plan								🟨 T	🟦							🟨
		Actual								🟨 E	🟩							🟨

7	Completed Chapter 2: Literature Review	Plan								R		🟦						
		Actual										🟩						
8	Discuss on Chapter 3: Methodology	Plan											🟦	🟦				W
		Actual								B			🟩	🟩				E
9	Completed Chapter 3: Methodology	Plan								R				🟦				E
		Actual								E				🟩				K
10	Preliminary Data	Plan								A					🟦			
		Actual								K					🟩			
11	Preparation for Final Year Project (FYP I) Presentation	Plan													🟦	🟦	🟦	
		Actual													🟩	🟩	🟩	
12	Final Year Project Presentation	Plan																🟦
		Actual																🟩
13	Submission Final Year Project (FYP 1) Report	Plan														🟦		
		Actual														🟩		

Final Year Project II (Gantt Chart)

No	Activity	Planning / Week	1	2	3	4	5	6	7	8	9	10	11	12	13	14	15	16
1	Chapter 4: Result Collect Data [100,110,111] • Constant Temperature [K] • Different Temperature [K] • Heat Flux [Mw/m^2]	Plan	🟦	🟦	🟦	🟦						🟨						🟨 S
		Actual	🟩	🟩	🟩	🟩	🟥	🟥	🟥	🟥	🟥	🟥 M	🟥	🟥	🟥			🟨 T
2	Progress Report	Plan								🟦		🟨 I						🟨 U
		Actual								🟩		🟨 D						🟨 D
3	Data Analyse • Density Distribution • Temperature Distribution	Plan		🟦	🟦	🟦	🟦	🟦	🟦	🟦	🟦	🟦	🟦	🟦	🟦			🟨 Y

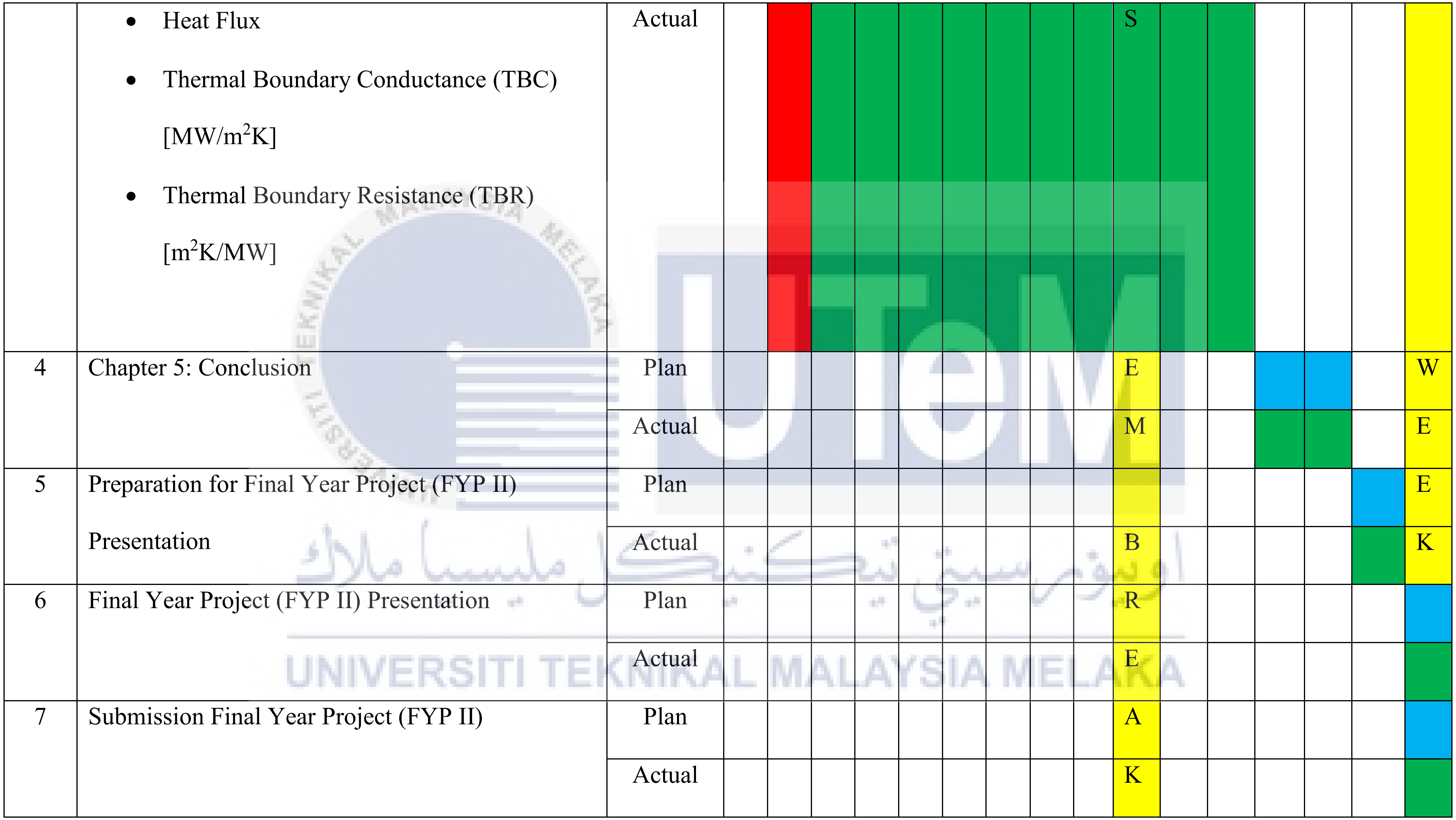

	- Heat Flux - Thermal Boundary Conductance (TBC) [MW/m^2K] - Thermal Boundary Resistance (TBR) [m^2K/MW]	Actual		🟥	🟩	🟩	🟩	🟩	🟩	🟩	🟩 S	🟩	🟩				🟨
4	Chapter 5: Conclusion	Plan									🟨 E			🟦	🟦		🟨 W
		Actual									🟨 M			🟩	🟩		🟨 E
5	Preparation for Final Year Project (FYP II) Presentation	Plan									🟨					🟦	🟨 E
		Actual									🟨 B					🟩	🟨 K
6	Final Year Project (FYP II) Presentation	Plan									🟨 R						🟦
		Actual									🟨 E						🟩
7	Submission Final Year Project (FYP II)	Plan									🟨 A						🟦
		Actual									🟨 K						🟩

Figure 1.2 Final Year Project I & II Gantt Chart

1.9 Outline Thesis

Throughout this research, it mainly focuses on the thermal rectification at the S-L interface of simple liquid in contact with FCC. To obtain the result for this research, the MD simulation are used in order to examined and study the influence and the effect of surface structure of solid on the thermal rectification at S-L interface of simple liquid and FCC.

The outline of this thesis is as follows:

In Chapter 2, the preliminary study and research on literature review is perform in order to obtain the information about the historical and methodological review of this research so that the theoretical framework on this research can be understand more detail.

In Chapter 3, it provides an outline of the methodology which including the simulation model and potential function which used to describe the model of the solid gold (Au) and liquid methane (CH_4). Other than that, the simulation condition for the model is elucidated in this chapter and the validation of density distribution is clarified and discussed in this chapter.

For Chapter 4, it elaborates on the thermal rectification at S-L interfaces in order to provide a detail understanding of the influence of directions of heat flows for the structure (100, 110, 111). Next, the data analyse for the density distribution, temperature distribution, heat flux, thermal boundary resistance (TBR) and thermal boundary conductance (TBC) is elucidated in this chapter for each of the structure (100, 110, 111).

In Chapter 5, the conclusion of this research is described and the summary of the result is elucidated.

CHAPTER 2

LITERATURE REVIEW

2.1 Introduction.

In this chapter, an overview of literature review is studies in order to understand the fundamental of molecular dynamic (MD) simulation and the thermal rectification at the S-L interfaces. The summary of the algorithm of the MD simulation, thermostat and barostat is discuses in this chapter. From here, the best selection of the algorithm, thermostat and barostat will be used in the MD simulation. The uses of periodic boundary condition (PBC) in the simulation system is explain in this chapter. The relevant detail about the ensemble, potential function, interfacial resistance, thermal rectification and the measurement of density, temperature as well as the heat flux is elucidated in this chapter.

2.2 History about Molecular dynamics Simulation

The first introduced molecular dynamic is Alder and Wainwright in the year of 1950’s to study the interaction of hard sphere (Theory of molecular dynaimc simulation, n.d.). Next, Rahman is the next major advance of the molecular dynamic in 1964 to carry out the first simulation using a realistic potential for liquid argon. Molecular dynamic simulation is the simulation that study and observe the physical movement of the molecule and atom which allowed it to interact for a fixed period of time and giving a view of the dynamic evolution of the system. The trajectories of atoms and molecules are determined by numerically solving Newton's equations of motion for a system of interacting particles, where the forces between the particles and their potential energies are often calculated using interatomic potentials or molecular mechanics force fields (Dr. Karina Kubiak, n.d.). Molecular dynamic simulation technique is mainly used in experimental procedures such as x-ray crystallography and nuclear magnetic resonance (NMR) structure determination.

2.3 Fundamental of Molecular Dynamics (MD) Simulation

In molecular dynamic simulation, the motion of particles in a simulation system is described by the Hamiltonian in the form of Newton's equation of motion by consider a set of *N* particles with position r and momentum p. Where by K and U are the kinetic and potential energy of the particles in the simulation system. U_i is the potential energy of the interaction between particles. P_i is the momentum of particle i. $\mathrm{m_i}$ is the mass of particle i. The equation (1.1) below is the Hamilton equation used to calculate the motion of particles:

$$H(p,r) = K + U = \sum_{i=1}^{N} \frac{{P_i}^{2}}{2m_i} + U_i \tag{1.1}$$

The equation of motion in equation (1.2) refers as the position $\dot{r}$ and momentum $\dot{p}$:

$$\dot{r} = \frac{\partial H}{\partial p} \qquad \dot{p} = \frac{\partial H}{\partial r} \tag{1.2}$$

The term *r* and *p* are refers as $\mathrm{ſ} = \{\mathrm{r}, \mathrm{p}\}$ and the time derivative is referring as:

$$\frac{d\mathrm{ſ}(\mathrm{t})}{dt} = iL\mathrm{ſ}(\mathrm{t}) \tag{1.3}$$

The term formula for iL is as below:

$$iL = \sum_i \dot{r}_i \frac{\partial}{\partial r_i} + \sum_i \dot{p} \frac{\partial}{\partial \dot{p}_i}$$

$$= \sum_i \dot{r}_i \frac{\partial}{\partial r_i} + \sum_i F_i(r) \frac{\partial}{\partial p_i} \tag{1.4}$$

The $F_i(r)$ in the equation (1.4) above refer as the force acting on the particle i. The equation (1.5) has a formal solution of:

$$f(t) = \exp(iLt)f(0) \qquad (1.5)$$

The term exp(iLt) in equation (1.5) is referring as:

$$\exp(g) = \sum_{n=0}^{\infty} \frac{g^{(n)}}{n!} \qquad (1.6)$$

The time propagator is referring as below. $G(\Delta t) = G^{-1}(-\Delta t)$ formula in equation (1.7) refer as the time reversible.

$$G(\Delta t) = e^{iL\Delta t} \qquad (1.7)$$

In molecular dynamic, phase space is referring as the momenta and unique position of each particle for a system of N particles. In other word, phase space also described as 6N dimensional spaced. In the system, each of the particle has three momentum variable (p_x,p_y,p_z) ranging from $-\infty$ to ∞ and three position variable which is in (x,y,z) ranging from $0 \; to \; L$. The part 6N number refers as the microscopic state of the system at time t. The variable of 6N describes every conceivable position and momentum combination of all particles in a mechanical system (Tuckerman, 2010). The figure 2.1 below shows two atoms inside the phase space. The green arrow vector indicates the momenta while the blue arrow vector indicates the position of the atom.

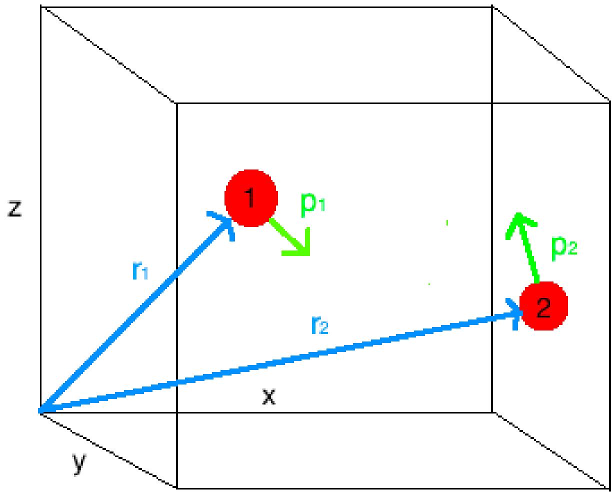

Figure 2.1 Phase space

2.4 Algorithm of Molecular Dynamics

Newton's equation of motion alone cannot be solved when involve a complex system but molecular dynamic algorithm is used in the simulation system to calculate the atomic force. It used to calculate trajectories of particles in molecular dynamic simulation. In 1791, this algorithm is first applied by Delambre, then recently by Loup Verlet in the 1960's for use in molecular dynamics (W.H, 2007). In molecular dynamics simulation, algorithm have regularly to be low of order that does not involve high storing of derivatives of position and velocities, this allow the time step to increase as much as possible without jeopardizing energy conservation (Neumann, 2004). The advantages of molecular dynamic algorithm are very simple and high accuracy for the position. In the molecular dynamic, there are five algorithms that normally used to calculate the atomic force which are Verlet algorithm, leap-frog algorithm, Velocity Verlet algorithm, Beeman's algorithm and (r-RESPA) revisable reference system propaganda algorithm. These five algorithms have its own function and these five algorithms are explained at the section below.

Figure 2.2 below represent the simplified flow chart of the standard molecular dynamic algorithm. At which the predictor stage and corrector stage are involve in this simulation. First, set the initial time, position and velocities of the atom as zero. At the predictor stage, the number of i is set in order to predict the position of the atom at that position and velocities. The forces can either in term of quantum mechanical $F = F[\varphi(r^{\rho})]$ or classical interatomic potentials $F = -\nabla V(r^{\rho})$ method. At the corrector stage, the position of the atom is adjusted based on the new a that obtain from the previous step. After the corrector stage, boundary condition, temperature and pressure are applied to the system if necessary. Next, the output physical quantities of interest are calculated. Then the time is move forward from the previous time step. Lastly, the step is repeated start from the predictor stage.

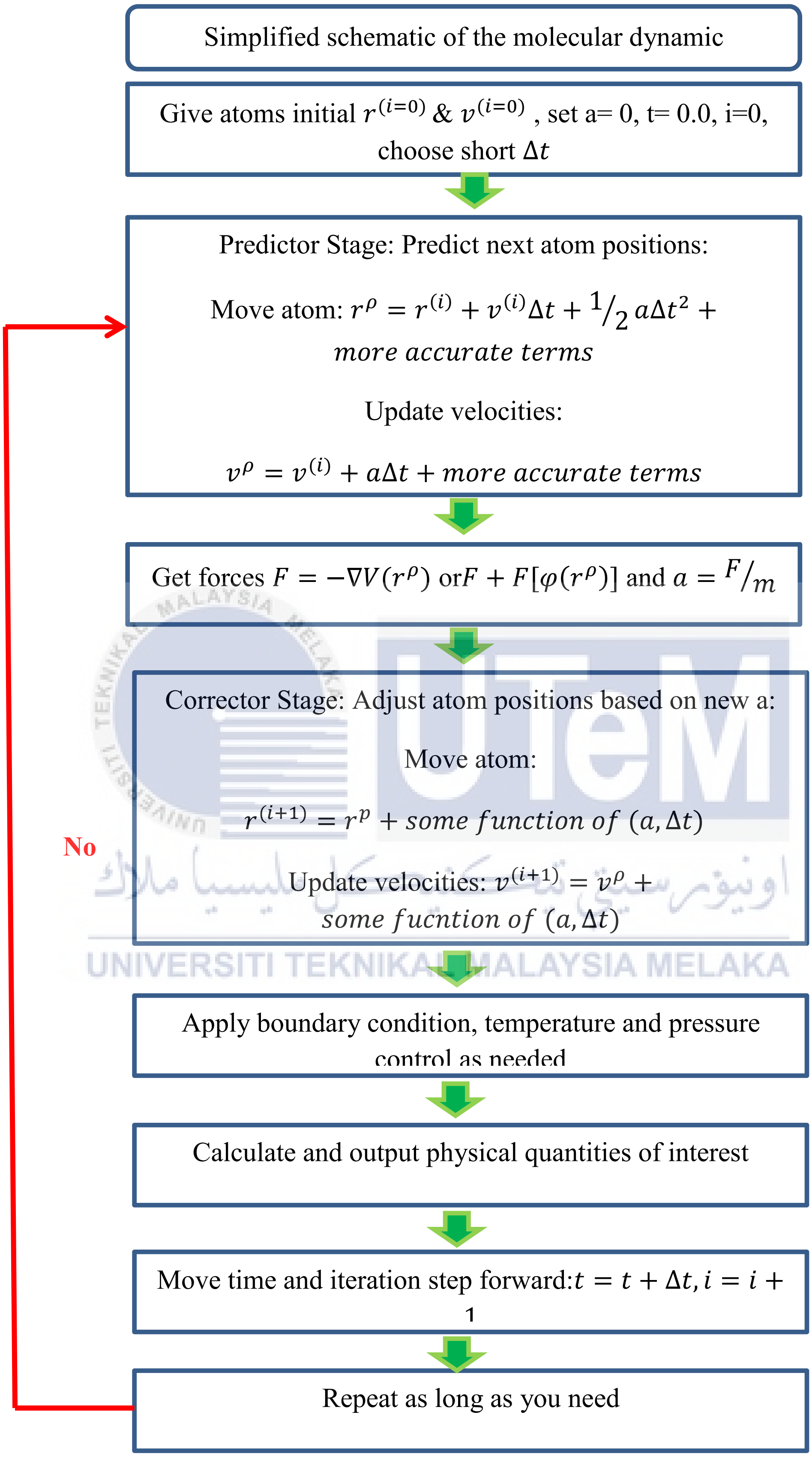

Figure 2.2 Simplified step of MD algorithm (张戈辉, 2017)

2.4.1 Verlet Algorithm

The Verlet algorithm in the molecular dynamic is a numerical method that used to integrate the Newton's equations of motion. The origin equation of Verlet algorithm is came from the two-third order Taylor expansion for the atom *i* positions (Dr. Karina Kubiak, n.d.). The equation (1.8) below refer as the one forward in time while the equation (1.9) below refer as the one backward in time.

$$r(t+\delta t) = r(t) + \frac{dr(t)}{dt}\Delta t + \frac{1}{2}a\delta t^2 + \frac{1}{6}\frac{d^3y}{dt^3}\delta t^3 \qquad (1.8)$$

$$r(t-\delta t) = r(t) - \frac{dr(t)}{dt}\Delta t + \frac{1}{2}a\delta t^2 - \frac{1}{6}\frac{d^3y}{dt^3}\delta t^3 \qquad (1.9)$$

The equation (1.8) and (1.9) is added together to form the basic form of the Verlet algorithm in equation (2.0) below:

$$r\,(\,t + \,\delta t\,) = 2r(t) - r(t-\delta t) + a(t)\delta t^2 \qquad (2.0)$$

The acceleration a is come from the equation (2.2) below:

$$F(r) = -\nabla U(r) \text{ and } F(r) = ma = m\frac{d^2r}{dt} \qquad (2.1)$$

$$a(t) = \frac{d^2r}{dt^2} = \left(\frac{1}{m}\right)\nabla U(r) \qquad (2.2)$$

Verlet algorithm are used to calculate the new position at specific time *(t + δt)* by using acceleration and position at specific time t and the position from time *(t - δt)*. The advantages of Verlet algorithm is it is straight forward and the storage requirement are modest but the precision and accuracy of the Verlet algorithm is just moderate if compare to another algorithm (张戈辉, 2017).

2.4.2 Leap-Frog Algorithm

The Leap-frog algorithm in the simulation is based on the Verlet scheme (Verlet, 1967). The Leap-frog algorithm in the simulation is used to calculate the velocities at half time step intervals. Based on the Leap-frog algorithm method, the (*v*) velocities keep leap over the (*r*) position and the (*r*) position leap over the (*v*) velocities as shown in figure 2.3. The advantage of leap-frog algorithm is the velocities are clear to calculate but the positions are not calculated at the same time as the velocities (张戈辉, 2017). Equation (2.3) and (2.4) represent Leap-frog algorithm.

$$r\ (t+\delta t) = r(t) + v(t+\tfrac{1}{2}\delta t)\delta t \qquad (2.3)$$

$$v\left(t+\tfrac{1}{2}\,\delta t\right) = v\left(t-\tfrac{1}{2}\,\delta t\right) + a(t)\delta t \qquad (2.4)$$

In equation (2.3) and (2.4) the r is refer as the position, v refer as the velocity,a refer as the acceleration, t is time, δt refer as the time step.

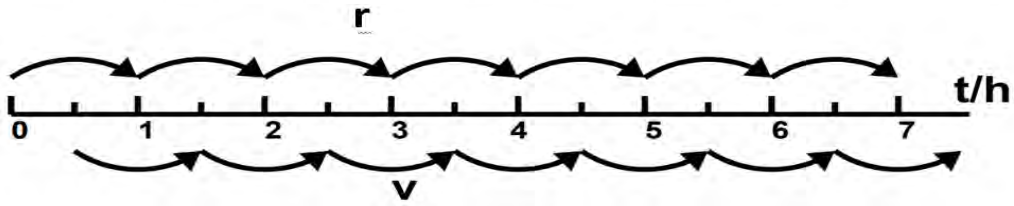

Figure 2.3 Leap-frog algorithm (Young, 2013)

2.4.3 Velocity Verlet Algorithm

Velocity Verlet algorithm generates a sequence of snapshot for the particle coordinates and velocities at all intermediate time δt. The advantages of Velocity Verlet algorithm are fast, accurate and time reversible. Equation (2.5) and (2.6) represent as the Velocity Verlet algorithms:

The position of the atom is updated every δt step in equation (2.5)

$$r(t+\ \delta t) = r[t + v(t)\delta t] + \frac{1}{2}\ a(t)\delta t^{2} \tag{2.5}$$

$$v(t+\ \delta t) = v(t) + \frac{1}{2}[a(t) + a(t+\delta t)]\delta t \tag{2.6}$$

In equation (2.5) and (2.6), r is the position, v refer as the velocity,a refer as the acceleration, t is time, δt refer as the time step.

2.4.4 Beeman's Algorithm

In 1973, the direct variant was published by Schofield as a personal communication from Beeman's which known as Beeman's method (P.Schofield, 1973). It is used for high number of particles in molecular dynamic simulation. In 1976, Beeman's had developed a class of implicit which is the predictor-corrector multi step method. This method refers as the direct variant of the third-order method in this class (D.Beeman, Some multistep methods for use in molecular dynamics calculations, 1976). The Beeman's algorithm is similar to the verlet algorithm that is this algorithm give a more precise and accurate expression for the velocities. But Beeman's algorithm is a complex expression compare to another algorithm (张戈辉, 2017). Equation (2.7) and (2.8) is standard form of Beeman's algorithm:

$$r(t+\ \delta t) = r(t) + v(t)\delta t + \frac{2}{3}\ a(t)\delta t^{2} - \frac{1}{6}a(t-\delta t)\delta t^{2} \tag{2.7}$$

$$v(t+\ \delta t) = v(t) + v(t)\delta t + \frac{1}{3}a(t)\delta t + \frac{5}{6}a(t)\delta t - a(t-\ \delta t)\delta t \tag{2.8}$$

In equation (2.7) and (2.8), r is refer as the position, v is the velocity, a is the acceleration (D.Beeman, Beeman's Algorithm, 2010).

$$v(t+\delta t)_{(predictor)} = v(t) + \frac{3}{2}a(t)\delta t - \frac{1}{2}a(t-\delta t)\delta t \qquad (2.9)$$

Equation (2.9) refer as the predictor step, which is the velocity at time $t = (t + \delta t)$are calculated from the positions (D.Beeman, Beeman's Algorithm, 2010).

$$v(t+\delta t)_{(corrector)} = v(t) + \frac{1}{3}a(t+\delta t)\delta t + \frac{5}{6}a(t)\delta t - \frac{1}{6}a(t-\delta t)\delta t \qquad (3.0)$$

Equation (3.0) refer as the corrector step, which is the acceleration at time $t = (t + \delta t)$ are calculated from the positions and predictor velocities.

2.4.5 Reversible Reference System Propagator (r-RESPA) Algorithm

In molecular dynamic, reversible reference system propagator (r-RESPA) algorithm is a time steeping algorithm that evolves the system state over time. In other word, (r-RESPA) method defines short range force as reference system force but for long range force correct only for the velocities (Saleman, 2017). Equation (3.1) below is the Liouville operator:

$$iL = \sum_i \dot{r}_i \frac{\partial}{\partial r_i} + \sum_i F_S(r)\frac{\partial}{\partial p_i} + \sum_i F_l(r)\frac{\partial}{\partial p_i} = iL_s + \sum_i F_l(r)\frac{\partial}{\partial p_i} \qquad (3.1)$$

The propagator equation (3.2) involves the slow varying of long-range force F_l .The time propagator in (r-RESPA) is factorized into:

$$G_{|S|}(\Delta t) = e^{(\Delta t/2)F_l(r)\frac{\partial}{\partial p}} \times e^{iL_s\Delta t} \times e^{(\Delta t/2)F_l(r)\frac{\partial}{\partial p}} \qquad (3.2)$$

The middle propagator is causes by short range force $F_s(r)$. Trotter factorization is involved in this case. Equation (3.3) below is the Trotter factorization:

$$e^{iL_s\Delta t} = [e^{(\delta t/2)F_s(r)\partial/\partial p} \times e^{(\delta t\dot{r}\partial/\partial r)} \times e^{(\delta t/2)F_s(r)\partial/\partial p}]^n \qquad (3.3)$$

In equation (3.3), the term δt is referring as $\Delta t/_{n}$ which n is selected in a way that stable dynamics is achieved in a system. The overall factorization propagator is given in the equation (3.4) below:

$$G_{|S|}(\Delta t) = e^{\left(\frac{\Delta t}{2}\right)F_l(r)\frac{\partial}{\partial p}} [e^{\frac{\left(\frac{\delta t}{2}\right)F_s(r)\partial}{\partial p}} \times e^{\left(\frac{\delta t\dot{r}\partial}{\partial r}\right)} \times e^{(\delta t/2)F_s(r)\partial/\partial p}]^n e^{(\Delta t/2)F_l(r)\frac{\partial}{\partial p}} \quad (3.4)$$

The previous value of long-range force $F_l\,(r)$ and short-range force $F_s(r)$ is used as an input for the following step. In each of one-time step, only one value is obtained for $F_l\,(r)$ and $F_s(r)$ which is only one evaluation of $F_l\,(r)$ and *n* number of $F_s(r)$.

(r-RESPA) is used to speed up or accelerate a simulation up to a factor on the order of 20 and 30 (M. Tuckerman, 1992). Single time step method is used to obtain result in a faster simulation speed. The time saving can be used to study the larger system that consumes longer simulation times. (r-RESPA) is very simple, accurate and stable to use and it need a decision of the part of the system to be integrated with which time step (Steven J. Stuart, 1996). (r-RESPA) in the system is decomposed into long range and short-range force component that show in equation (3.5).

$$F(r) = F_s(r) + F_l(r) \quad (3.5)$$

2.4.5.1 Short Range Force

In (r-RESPA), the short-range force is defined as the time step to be used in a calculation of molecular dynamic which is given by the equation (3.6) below:

$$F_s(x) = s(x)F(x) \quad (3.6)$$

In equation (3.6), *s(x)* is the sigmoidal function. *s(x)* is unity at short inter-particle separation. Sigmoidal function represents cubic spline which is the switching point and skin-depth that can be optimized. The cost of CPU would be small for the short-range force because each particle only interacts with it nearest neighbours (Berne, 1999).

2.4.5.2 Long Range Force

For long range force in (r-RESPA), it is costly to calculate. To reduce the cost of the simulation, the strategy into the (r-RESPA) propagator factorization and the non-reversible RESPA are introduced. The equation (3.7) represent as the long-range force:

$$F_l(x) = [\,1 - s(x)]F(x) \tag{3.7}$$

In equation (3.7), *s(x)* in the long-range force equation represented as sigmoidal function. *s(x)* is 0 at large inter-particle separation. In updating of data, the position will be updated by using only smallest time-step. Meanwhile, the velocities will be updated on two different time scales. From here, this step allows one to update the expensive long-range force much less frequently than updating the cheap short-range force and this save CPU time without sacrificing the accuracy. This accelerate up as much as 400% even for the simple system like a liquid which consisting of atoms interacting through a Lennard-Jones potential (Berne, 1999).

2.4.6 Overview of the MD Algorithm

Table 2.1 Types of algorithm

Type of algorithm	Advantages	Disadvantages
Verlet Algorithm	• Straight forward • Modest storage requirement	• Precision and accuracy are moderate
Leap-Frog Algorithm	• Velocities clear to calculate	• Position are not calculated at the same time as the velocities
Velocity Verlet Algorithm	• Time reversible • Same order as Verlet algorithm	• No compromise precision
Beeman's Algorithm	• Accurate and precision expression for velocities	• Complex expression
Reversible Reference System Propagator Algorithm (r-RESPA)	• Simulate a complex system in shorter time. • Accurate • Simple • Stable	-

In table 2.1, it shows the advantages and disadvantage for each types of the MD algorithm. The Verlet algorithm is very straight forward and only require modest storage to store but the precision and the accuracy is just moderate. For the Leap-Frog algorithm, the velocities are easily to calculate but the position are not calculated as the same time as the velocities. As for Velocity Verlet Algorithm, its order is the same as the Verlet algorithm but it can perform time reversible. In MD algorithm, Beeman's algorithm have the most complex expression compare to other algorithm but it can obtain the most accurate and most precise expression to obtain the velocities. Next, the Reversible Reference System Propagator Algorithm (r-RESPA) are easily to uses, stable, accurate and able to reduce the simulation times. As for the present simulation, (r-RESPA) algorithm is chosen to simulate the model as it able to get accurate result and able to simulate the model in a shorter time.

2.5 Ensemble

An ensemble is defining as the collection of all possible system which consisted of different microscopic states but have the same thermodynamic state or macroscopic state. The thermodynamic states in the system are defined as a small set of parameters which is the temperature (*T*), pressure (*P*) and number of particles (*N*). In molecular dynamic, there are four different ensembles used which is the canonical ensemble (*NVT*), microcanonical ensemble (*NVE*), grand canonical ensemble (μVT) and isobaric-isothermal ensemble (*NPT*). Each of the ensembles had its own characteristic. As for *NVT* ensemble, it describes as the collection of all of the system in thermodynamic state which characterized by a constant number of atoms (*N*), constant volume (*V*) and constant temperature (*T*). For *NVE*, it is identical to an isolated system which the thermodynamic state is indicate by a constant number a atoms (*N*), constant volume (*V*) and constant sum of energy (*E*). At which the sum of energy in *NVE* ensemble consist of kinetic and potential energy. Next, (μVT) ensemble is referring as constant chemical potential (μ), constant volume (V) and constant temperature (T) in thermodynamic states. Lastly, (NPT) ensemble is characterized by a constant number of atoms (N), constant pressure (P) and a constant temperature (T) (Theory of molecular dynaimc simulation, n.d.). To maintain the temperature in the system, thermostat is applied to the system. Meanwhile, to maintain the pressure in the system a barostat is used in the system so that the pressure is kept constant. The pressure of the system is control via shell particle (S.Corti, 2013).

Ensemble average consumes less simulation time but exhibits the same overall computational effort. Phase space sampling is the information collected during atomic simulation and this can be done by using ensemble average method. An ensemble average is the average taken over a large number of replicas of the system considered simultaneously. The ensemble average is given in equation (3.8).

$$A._{ensemble} = \iint dp^N dr^N A(p^N . r^N)\rho(p^N . r^N) \qquad (3.8)$$

Where (p^N, r^N) is the observable of interest as a function of momenta p, the position r of the system. The probability density of the ensemble is given in equation (3.9).

$$\rho(p^N . r^N) = \frac{1}{Q}\, exp\,[-\frac{H(p^N . r^N)}{k_B T}] \qquad (3.9)$$

Where H is the Hamiltonian, T is the temperature, k_b is Boltzmann's constant and Q is the partition function in equation (4.0).

$$Q = \iint d\,p^N\,dr^N\, \exp[\,-H\frac{p^N . r^N}{k_b T}\,] \qquad (4.0)$$

In order to calculate an ensemble average, the molecular dynamic simulation must pass through all possible states corresponding to the particular thermodynamic constraints. (http://chemistry.umeche.maine.edu/CHY431/MolDyn2.html, 2012)

2.6 Periodic Boundary Condition (PBC)

Periodic boundary condition (PBC) is mostly used in computer simulation and modelling. It used to simulate an infinite system. PBC normally measured by using a unit cell in a large system. In molecular dynamic simulation, periodic boundary condition (PBC) is used to calculate the mixture, liquid and bulk glass and to eliminate surface effect (NPTEL, 2012). Application that uses PBC is to simulate solvated macromolecules in a bath of explicit solvent. The used of PBC also avoid problem with the boundary effect caused by finite size and also make the system more like an infinite one, at the cost of possible periodicity effects. (mabraham, 2013). PBC are divided into 2 system which are finite system and macroscopic system. For finite systems, it uses open boundary condition which is no boundaries at all just N particles in space. As for macroscopic system, it can handle a larger number of particles which is approximate of 10^{23} in simulation (Physics 5403: Computational Physics, -). Figure 2.4 below is the periodic boundary condition of molecules in each cell.

The highlighted cell in figure 2.4 is called as the basic cell and the other 8 cell that surround the basic cell is called imagery cell. The lines that separating each cell in figure 2.4 are represented as the boundary. Each particle in the cell is free to cross the boundary of the cell but the movement of each particle in the imagery cell and the basic cell are similar. If the particles of the basic cell move out from the basic cell through the top boundary, then an identical particle of the imagery cell will move in to the basic cell through bottom boundary.

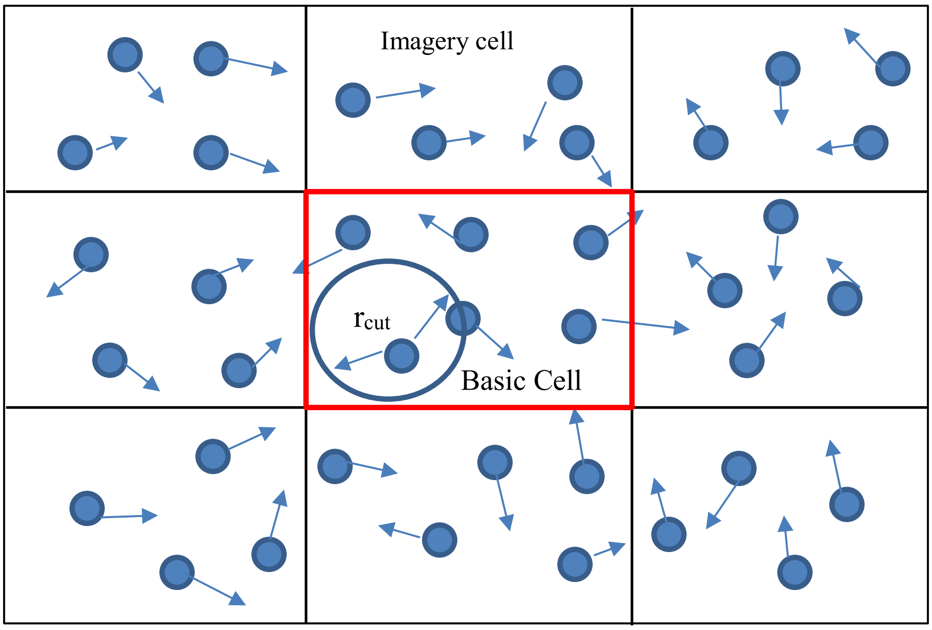

Figure 2.4 Periodic Boundary Condition

2.7 Thermostat & Barostat

In the molecular dynamic (MD) simulation, the Thermostat is used to regulated the temperature of the simulation condition so that the temperature of the simulation condition is near to the desired setpoint. Normally the thermostat that used in MD simulation which is the Nosé thermostat, Nosé-Hoover thermostat and velocity-scaling method. As for the Barostat, the function of the Barostat is used to maintain the pressure of the simulation condition so that the pressure of the simulation condition is maintain. The most common Barostat used in MD simulation which is the Berendsen Barostat, Andersen Barostat and Rahman-Parinello Barostat. But as for this research, the velocity scaling method is used as thermostat and Anderson Barostat is used as Barostat when perform a simulation for the model.

2.7.1 Thermostat

In the molecular dynamic simulation, thermostat is to help the sample simulation from the correct ensemble which is the canonical ensemble (*NVT*) or isobaric-isothermal ensemble (*NPT*) by modifying the temperature of the system in some of the cases (Mabraham, 2012). A variety of thermostat techniques are available to add and remove energy from the boundaries in the molecular dynamic system (Zhao, n.d.). There are two methods that used in thermostat which is the velocity scaling method and extended system method. In extended system method, the simulation system is coupled with a heat bath which comes with certain degree of freedom. Nose Hoover thermostat is one of the extended systems methods used in simulation. Meanwhile, the velocity scaling method is the direct method used in thermostat to control the temperature in the system.

2.7.2 Nosé Thermostat

Nosé devised a useful way of maintaining a system at a constant temperature by a reformulation of the equation of motion and this can be rigorously formulated by using the Lagrangian approach to classical mechanics. Nosé approach was to add two additional degrees of freedom to the system and acts thermal reservoir (M.S.Shell, 2009).

2.7.3 Nosé-Hoover Thermostat

In molecular dynamic simulation, Nosé-Hoover thermostat is a deterministic algorithm for constant temperature and it was created by Nose in 1984 and further improvement by Hoover in 1986 (M.S.Shell, 2009). Other part than that, Nose-Hoover thermostat also provides a method to simulate a system which is in the *NVT* ensemble but induce oscillation in the dynamic (dmarendu, 2012). Therefore, Nosé-Hoover is the most accurate and precision methods for constant temperature and is the most common use in molecular dynamic simulation.

2.7.4 Velocity Scaling Method

In thermostat, velocity scaling method of woodcock is represented as direct method (L.V.Woodcock, 1971). Velocity scaling method is the method that used to control the temperature in the system by scaling the velocity of each particle closer to the desire temperature so that the kinetic energy of the particle is constant (Saleman, 2017).

2.7.5 Barostat

In the molecular dynamic simulation, Barostat is used in the simulation to control the pressure of the system. A Barostat technique used in the molecular dynamic simulation consists of Berendsen Barostat, Andersen Barostat and Rahman-Parinello Barostat.

2.7.6 Berendsen Barostat

In molecular dynamic simulation, Berendsen Barostat is use for controlling the pressure in the system. The Berendsen Barostat also adds an extra term to the equations of motion which effects the change in pressure (Berendsen, 2014).

$$\frac{dP(t)}{dt} = \frac{P_{md-}P(t)}{\tau_p} \tag{4.1}$$

In equation (4.1), $P(t)$ is the instantaneous pressure, P_{md} is the desired pressure, and τ_p is the Barostat relaxation time constant. Figure 2.5 below are Berendsen Barostat relaxation time step graph:

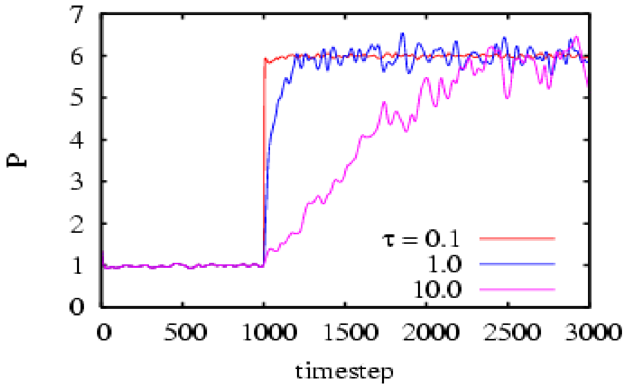

Figure 2.5 Berendsen Barostat relaxation time step graph (Pages.drexel.edu, n.d.)

2.7.7 Andersen Barostat

Andersen Barostat is the extended system method that involves coupling the system to an external variable *V*, the volume of the simulation box (Molecualr Dynamic, n.d.). The Nosé-Hoover Barostat and the Martyna-Tuckerman-Klein Barostat are both based on the Andersen Barostat. The Andersen method was developed to adjust the pressure in a simulation of interacting particles (Ruhle, 2008). Anderson Barostat is used appropriate for liquid but not for shear stress in liquid. By the way, Anderson Barostat can change the volume of the liquid by rescaling the position and to allow the size of the box to fluctuate but not change the shape (Kieffer, n.d.).

2.7.8 Rahman-Parinello Barostat

Rahman-Parinello Barostat only can be used in a solid molecule in the molecular dynamic simulation. Other than that, Rahman-Parinello Barostat allows the shape to change. Rahman-Parinello is use to simulate the phase transformations in solid (Kieffer, n.d.).

2.8 Potential Function & Model

In MD simulation, the potential function is used to described the interaction between the molecules and atoms while the model is used to represent the molecules or atoms. In this section, the potential function used for the solid model and liquid model is elucidated. In general, the potential function used to describe the solid model are the Morse potential, Embedded Atom Model (EAM) and Lennard-Jones (LJ) Potential. Meanwhile, the most famous potential used to describe the liquid model is the LJ potential. Each of the potential function used in the simulation have their own advantage and disadvantages based on the condition.

2.8.1 Solid Model

In 1929, the Morse potential is name after the physicist name Philip M.Morse and frequently used for modelled solid wall or crystal due to its simplicity form that is only three fitting parameter. Morse potential is used to study the atomic and configuration properties of solid. It used to calculate the formation energy of vacancies and interstitial atoms and to calculate the energy of stacking faults in solid (E.V. Kozlov, 1971). In equation (4.2), $\Phi\ (r_{ij})$ is the interaction energy between the atoms i and j that were separated by the distance r_{ij}. As for term D_e , D_e is the well depth that defined the relative to the dissociated atoms. Meanwhile the term r_y is the coordinate perpendicular to the surface. Whereby r_u is the equilibrium bond distance. Figure 2.6 is the Morse potential graph. The potential formula for the solid walls modelled is given below:

$$\Phi(r_{ij}) = D_e\ [e^{-2a\,(r_y - r_u)} - 2e^{a(r_y - r_u)}] \qquad (4.2)$$

In equation (4.3), α is refer as control the width of the potential. The larger the α value, the smaller the well. K_e is the force constant at the minimum of the well. The formula is obtained from the equation (33) below:

$$\alpha = \sqrt{\frac{K\,e}{2D}} \tag{4.3}$$

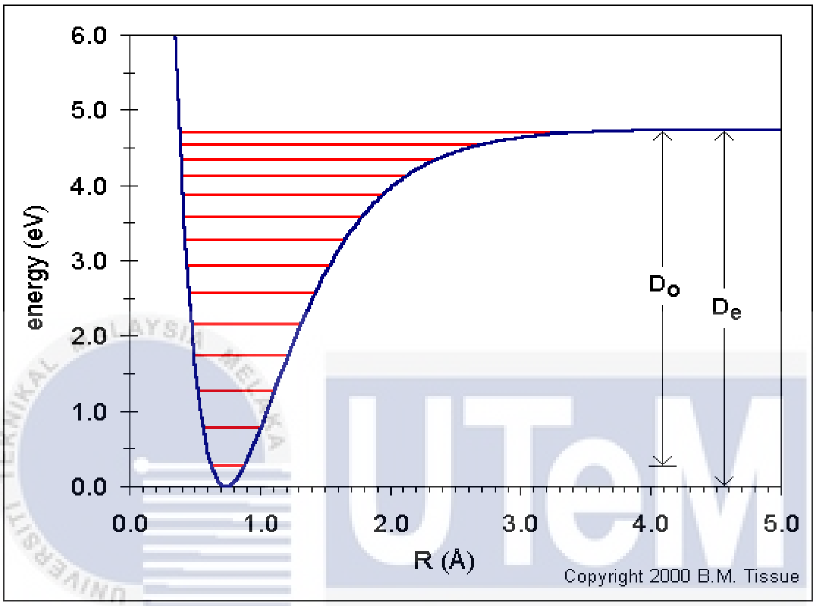

Figure 2.6 Morse potential graph (Chemistry, 2015)

In figure 2.6, it represents as the Morse potential graph. The diatomic molecules are created if the two atoms approach each other closely to form a bond. In this case, the potential energy of the diatomic molecules is lower than that of the reactants. The minimum energy with a potential energy curve is called as potential well. In figure 2.6, De is refer as the well depth and D_o is refer as the dissociation energy which is slightly different from form the well depth De. The curve in the figure 2.6 is calculated based on the Morse potential. The energy level in the figure 2.6 is calculated by using the harmonic oscillator model with the first an-harmonic correction. For vibration energy level in the figure 2.6, it calculated by using the harmonic oscillator model (Definition of Morse Potential, 2017).

$$E_v = \left(v + \tfrac{1}{2}\right) V_e - (V + \tfrac{1}{2})^2 v_e x_e + (v + \tfrac{1}{2})^3 v_e y_e + higher\ terms \qquad (4.4)$$

In equation (4.4), v refer as the vibration quantum number, $x_e$and y_e are the first and second anharmonicity constant. If v is equal to zero level, it means the vibrational is in ground state.

Murray Daw and Mike Baskes are the researchers that develop the Embedded Atom Model (EAM) method in 1983 which based on the density functional theory. Embedded Atom Model (EAM) is the model that explains the energy between the atoms in the system which called an interatomic potential. EAM potential is mostly used or applies for alloys and metals (Basjes, 1984). Other than that, EAM potential is not reliably describing the nanostructure because it often incorrectly describes the inward or outward relaxation of surface layer. EAM potential in the simulation are consists of three constraints on elastic constants that are inconsistent with the experiments. The advantages of EAM potential used in the simulation which are the unphysical constraints on elastic constants is eliminated and the bond saturation which causes the surface bonding is better represented (Huang). Next, EAM force field in the simulation gives a computationally efficient explanation of thermal properties and structural behaviour of metallic systems. The calculations of EAM in simulation are able to span length and time scales unreachable to the method of first principle (Embedded Atom Method (EAM) Simulation in the MedeA® Environment, 2012). EAM defined the condition of an atoms placed in a defined electron density and it used to explain the significant portion of the physical reality of metallic bonding which based on the effective theory of Lang and Norskov (Lang, 1980). In equation (4.5) described as the total energy of the system as two additive term, a pairwise sum of interactions between atoms and a term which describe the electron density of each atomic site.

$$U_{metallic} = \sum_{i=1}^{N-1} \sum_{j=i+1}^{N} V(r_{ij}) + \sum_{i=1}^{N} F(\rho_i) \qquad (4.5)$$

$$\rho_i = \sum_{j=1}^{N} \varphi_j(r_{ij}) \qquad (4.6)$$

In equation (4.5), $U_{metallic}$ represent as the total energy of the system while i and j represent as the unique pairs of atoms within the N atoms of the system. $V\left(r_{ij}\right)$ is a pairwise potential, r_{ij} is the interatomic separation, $F(\rho_i)$ is represent as the embedding function for atom i which is based on the electron density $\rho_i$of the atom. The term ρ_i is obtained by using equation (4.6).

In molecular dynamics, Lennard-Jones (LJ) potential function is the most famous potential used for simple liquid due to its simplicity form which easily to evaluate both theoretical and computer simulation, and yet to proves to capture much of the fundamental physics. In certain case, LJ neglect the higher order dispersion interaction which is r^{-8} and r^{-10} attraction and 3-body interaction which provide surprisingly good results for the liquid properties of system of closed-shell atoms for those which contain a high degree of spherical symmetry such as methane (Hoef, 2000). LJ potential may prove correct if a temperature-dependent well-depth parameter $\in (T)$ is used (Kofke, 1995) (Teja, 1996). But for the LJ potential used in solid model is different from the liquid model. In the past studies, there are a lot of studies regarding about the determination of free-energy of the LJ solid. Such as Gilmer and Broughton had studied the expression for the free energy by the thermodynamic integration of the internal energy from the harmonic crystal but only applied for P=0 isochore (Gilmer, 1983) . Other than that, Lacks and Shukla had proven an expression for the anharmonic free energy from molecular dynamics simulation and perturbation theory in the density range $\rho = 0.864$ to $\rho = 1.0$ and temperature range $T = 0$ to $T = 0.5$ which below the temperature triple point (Shukla, 1996). Hence, this is not suitable to solid-liquid (S-L) coexistence properties. Lisa and Vacek considered the solid phase of diatomic by using LJ models. Next, the most interesting part of LJ model in solid it provides an ideal starting point for the theoretical and computation study of simple polymer chains (E. SANZ, 2013). In LJ system, the solid phases are assumed to be a face centered cubic (FCC) lattice (Travesset).

2.8.2 Liquid Model

The Lennard-Jones potential formula is created by John Lennard-Jones in 1924. Lennard-Jones potential formula is used for liquid modelled in this project. Due to its computational simplicity, the Lennard-Jones potential is used extensively in computer simulations even though more accurate potentials exist. The Lennard-Jones model consists of two parts that is the smoother attractive term and the steep repulsive term. The steep repulsive term is the term of short-range repulsion due to overlap of the electron clouds that form purely phenomenological while the term for the smoother attractive is the Van-der Waals attraction between neutral atoms which is induce dipole-dipole. The Lennard-Jones is a mathematically simple model that approximates the interaction between a pair of neutral atoms (Naeem, Lennard-Jones Potential, 2017). The Lennard-Jones potential formula is given below:

$$U^{LJ}(r_{ij}) = 4\,\varepsilon_{ij}\overbrace{(\frac{\sigma_{ij}}{r_{ij}})^{12}}^{\boxed{\text{Steep repulsive term}}} - \overbrace{(\frac{\sigma_{ij}}{r_{ij}})^{6}}^{\boxed{\text{Smoother attractive term}}} \qquad (4.7)$$

In equation (4.7), U^{LJ} is the intermolecular potential between two atoms. ε is the well depth and a measure of how strongly the two particle attract to each other. σ is the distance at which the intermolecular potential between the two particles measure from zero. r_{ij} is the distance of separation between both particles that measured from the center of one particle to the center of the other particle (Naeem, Lennard-Jones Potential, 2017). Figure 2.7 below is the Lennard-Jones Potential graph:

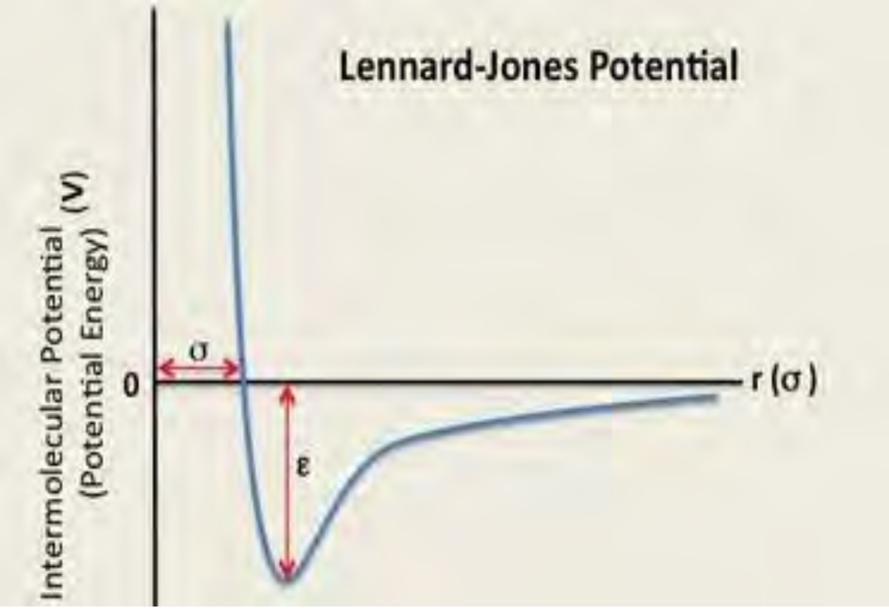

Figure 2.7 Lennard-Jones potential graph (Naeem, Chemostry LibreTexts, 2017)

Based on figure 2.7, it represents the Lennard-Jones potential graph. Equation (4.7) describes both the attraction and repulsion between the non-ionic particles. At which the term $(\frac{\sigma_{ij}}{r_{ij}})^{12}$ refer as the repulsive force between particles while the term $(\frac{\sigma_{ij}}{r_{ij}})^{6}$ refer as denotes attraction in equation (4.7) (Naeem, Chemostry LibreTexts, 2017). In figure 2.7, the deeper the well depth, the stronger the interaction between the two particles. When the bonding potential energy is equivalent to zero, the distance of separation of r will equal to σ. Zero bonding potential energy is referring as the two non-bonding particles to coming together and interacting to each other is zero.

2.9 Interfacial Resistance

Interfacial resistance is known as thermal boundary resistance (TBR) or Kapitza resistance. In the year of 1941, the interfacial thermal resistance was first discovered by

Kapitza when experiment the super fluidity of He II. Kapitza resistance is the resistance of a heat flow across the two interfaces that produce a temperature discontinuity when a constant heat flux is apply across an interface. The Kapitza resistance in the present simulation is calculated based on the Fourier's law.

$$Q = \frac{\Delta T}{R} = G\Delta T \tag{4.8}$$

In equation (4.8), Q is represent as the heat flux applied across the interface, ΔT is the temperature drop at the interface, R is the thermal boundary resistance and G is the thermal boundary conductance.

Kapitza resistance is caused by carrier scattering at the interface which the type of carrier scattered is depend on the materials governing at the interface and it also exist at perfect interface. Such as for metal-metal interface, the electron scattering effect will dominate the Kapitza resistance as the electron in the metal are the primary thermal energy carriers. The probability of phonon transfer is depending on the available energy state on material A and material B.

There are two theoretical developed to explain the interfacial thermal resistance at S-L interface namely AMM & DMM. AMM & DMM are explained in term of phonon mismatch & scattering at the S-L interface. Below are the detail explanations of DMM & AMM at the S-L interface.

2.9.1 Acoustic Mismatch Model (AMM)

In the year of 1952, khalatnikov used acoustic mismatch model to predict the thermal rectification at solid-solid (S-S) interface (Shi, 2016). Acoustic mismatch model (AMM) only valid for perfect interface at very low temperature below 7K (N.A. Roberts, 2010).

Figure 2.8 shown sample of AMM used in thermal rectification, *l*, t_1, t_2 represent as the transmission of phonon across the two different material. Based on figure 2.8, partially of the transmission of phonons is reflected away from the interface while partially of the phonon is absorbed into the interface. The refracted and reflected of phonon in AMM is due to the different density of two contact materials. The transmission of phonon in AMM is based on acoustic impedance of the two materials (N.A. Roberts, 2010). Acoustic impendence is used to predict the transmission of phonon at the interface. The angle of transmission phonon is based on Snell's law (AMRIT, 2014). Equation (5.0) below represent as the acoustic impendence used to predict the transmission of phonon in AMM. Equation (5.1) represent as Snell's law used in AMM.

$$Z = \rho c \tag{4.9}$$

$$\alpha_{1\to2}(\theta) = \frac{4Z_1Z_2}{(Z_1Z_2)^2} \tag{5.0}$$

$$\frac{\sin\theta_1}{c_1} = \frac{\sin\theta_2}{c_2} \tag{5.1}$$

In equation (4.9) and (5.1), ρ represent as density while *c* represent as the speed of sound. In equation (4.9), *z* represent as the acoustic impedance of the material.

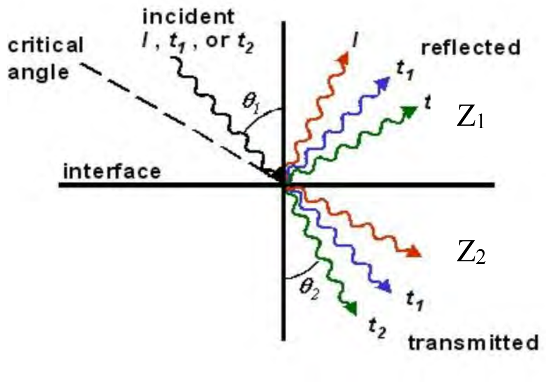

Figure 2.8 Acoustic Mismatch Model (AMM) (Shi, 2016)

2.9.2 Diffuse Mismatch Model

In the year 1989, Swartz and Pohl used Diffuse Mismatch Model (DMM) to predict the phonon transport between the two dissimilar solid. In DMM, the temperature range is much wider compare to AMM. DMM used to apply for the rough interface and to predict the phonon diffuse scattering at the interface. In diffuse scattering, a phonon loses it type of branch. The rough or diffuse interface resulted in a reduced rectification effect as result of increasing of inelastic scattering at the interface. In some case of DMM known as the Phonon Radiation Limit (PRL), the probability transmission of phonon is unity resulting in perfect transmission at the interface.

Figure 2.9 represent as Diffuse Mismatch Model (DMM). In figure 2.9, *r* represents as the transmission of phonon in DMM. The transmission of phonon in DMM is based on the ratio of the material density state and the phonon group velocity. In DMM, materials which have different phonon spectra can exhibit phonon transmission in one direction and reflection in the opposite direction due to the availability of phonon frequencies in the material. In thermal rectification, inelastic scattering allows the phonon to transmit through the interface. Inelastic scattering at interface is proven to increase with temperature and imperfection (diffused atoms) at the interfaces (N.A. Roberts, 2010). Equation (5.2) represent as transmission of phonon in DMM (Phillpot, 13). In equation (5.2), $D(\omega)$ represent as phonon density of states.

$$t_{AB}(\omega) = \frac{D_B(\omega)}{(D_A(\omega)+D_B(\omega)} \qquad (5.2)$$

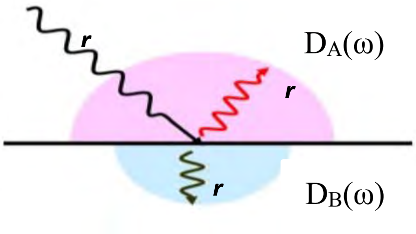

Figure 2.9 Diffuse Mismatch Model (DMM) (Shi, 2016)

2.10 Thermal Rectification

Thermal rectification is the influences of heat flow direction on the characteristic of thermal energy transfer between the two contacting surfaces. The contacting surfaces can either be in S-S or S-L. As for the present simulation model, the transfer of heat flow from solid to liquid is transfer via conduction. Section below is the pass studies of thermal rectification for the solid-solid interface and solid liquid interface.

2.10.1 Solid-Solid (S-S) Interface

At the start, the thermal rectification at solid-solid (S-S) interface was first explore by Starr in the years of 1936 when investigating the electrical rectification characteristics of Copper and Cuprous Oxide interface. Starr notice that it not only exhibits electrical rectification might as well exhibit thermal rectification. In years of 2002, the thermal rectification of S-S interface is further reintroduced by Terraneo et.al and C.W Chang which used a solid-state thermal rectifier system in simulation and experimental to study on the thermal rectification at S-S interface. Terraneo presented 1D non-linear lattice in simulation (M. Terraneo, 2002) while C.W Chang conducts experiment of non-uniformly mass loaded nanotubes in year 2006 (C.W. Chang, 2006). In year of 2004, Li et.al simulated a non-linear lattice and calculated a difference in conduction between the two directions to be 100 times that conduct by Terraneo. Next, the rectification in carbon nanotube intra-molecular junctions is demonstrated by Wu and Li by using molecular dynamic (MD) method in years 2008 (G.Wu, 2007). The large of structural asymmetry in solid enhance the thermal rectification efficiency (Nuo Yang, 2001). In the past studies, there are several ideas had been proposed to modified the surface of solid including flatness, bulk mechanism and thermal potential barrier between material contacts in order to studies on the thermal rectification at the S-S interface.

2.10.2 Thermal Potential Barrier

In year 1961, Rogers discover the rectifying effect in aluminium and steel interface. At which Rogers argue that the rectifying effect is cause by the difference in the work function of the two materials (aluminium and steel) (Rogers, 1961). The work function is called as the minimum thermodynamic work (energy) requires to remove an electron from the solid to a point in the vacuum immediately outside the solid surface. Rogers also did replace the aluminium with copper to test the validity of the argument of the warping at the interface. From here, Rogers found that the copper and steel have a greater rectification compare to aluminium and steel system. Based on Rogers, a larger difference of thermal conductivity k result in greater warping and therefore produces in greater rectification. The thermal potential barrier is believed to link with the work function of the materials in contact. Equation (5.3) defines as the work function.

$$W = -e\emptyset - E_F \tag{5.3}$$

In equation (5.3), $-e$ is the charge of an electron, $\emptyset$ is the electrostatic potential in the vacuum vicinity at the surface and E_F is the electrochemical potential of electrons inside the material.

In 1962, Moon and Keeler developed a model to show a difference in material work functions could result in thermal rectification. Their model is used to predict the greater transport in the direction of decreasing work function (step down) as opposed to increasing work function (step up) when a thin layer is present in between the two metal (R.N.Keeler, 1962). In 1970, Thomas and Probert observed the thermal rectification by conduct a series of experiments between dissimilar and similar material (S.D.Probert, 1970).

2.10.3 Bulk Mechanism and Metal

Thermal rectification exists in bulk system normally composed of metal or metal oxide. In bulk system, the thermal rectification is dependent of the surface characteristics such as the flatness and roughness of the surface as well as bulk material properties (N.A. Roberts, 2010).

In metal systems, the thermal energy transported mainly from the electron while the oxide or insulator is phonons. These two materials have different carrier (electrons and phonons) when it come in transport of thermal energy. At the interface of the metal, the electron from the metal must scatter with phonons then only can be transmitted into insulator or reflected back into the metal at the interface. The scattering of electron-phonon and phonon transmission lead to an effective contract resistance at the interface which is given by the equation (5.4) below.

$$R_C = R_{e-p} + R_{pt} \tag{5.4}$$

In equation (5.4), R_{e-p} is the resistance due to electron-phonon scattering and R_{pt} is the resistance due to reflection or transmission of phonons. At the interface, a temperature jump (TJ) exists due to the localized resistance.TJ exists is caused by non-equilibrium scattering rates of electron-phonons at the metal interface. At which the energy transfer from electron to phonons are differ from the energy transfer of phonon to electron (N.A. Roberts, 2010).

2.10.4 Solid-Liquid (S-L) Interfaces

Smoluchowski is the first person to explore the temperature jump at solid-liquid (S-L) interface when heat flux is applied (MS., 1898). In year 1941, Kapitza had discovered the phenomenon of interfacial thermal resistance when conducting experimental investigation of super fluidity of He II (Pollack, 1969). Based on Hu et al, the thermal rectification at S-L interface was influenced by the modified surface (M. Hu, 2009). Other than that, one of the researches had been studies by Murad et.al at which the thermal rectification at S-L interface is depend on the mass density and interfacial thermal resistance (S. Murad, 2012) (S.Murad, 2014). Several investigations had been studies in the past to look into the molecular interaction at the interface. At which Ohara et.al had studies on the transfer thermal energy at S-L interface of three species of sheared liquid contacting with three different of crystal planes (T.Ohara, 2005). These studies are utilized monoatomic liquids and two types of rigid diatomic molecules. Next, the investigation of thermal energy transfer at S-L interface between the systems of liquid without shear and with shear had been studies by Khare et.al (R.Khare, 2006). From these studies, the model liquid used in the systems is assumed strong and weak interaction between the solid and liquid molecules at which contact only the surface of (100) crystal plane. Although there are a lot of studies and investigation in the past about the characteristic of thermal transfer at S-L interface but most of the investigation failed to include the influence of heat flow direction at the interface. So, in the present study, the influence of heat flow at the interface is considered.

In term of manipulation, the structure of the solid is hard to manipulate due to it fix structure which make the thermal rectification for the devices challenging but as for liquid it is easier to manipulate by changing the pressure and temperature of the liquid. Through molecular dynamics simulation for (S-L) interface, thermal resistance cannot be ignored although system size is small. The thermal resistance is found to drastically drop with stronger (S-L) interaction and sharply decreased as the wettability of liquid increase (KIMURA, 1999). The larger the asymmetry is, the more obvious the thermal rectification. By manipulating the temperature of the solid or liquid give better opportunities for the rectification in the (S-L) system (K.Puri, 2012). From here this opens up a lot of application that use thermal rectification.

2.11 Measurement

In this section, the measurement of density distribution, temperature distribution and heat flux in the simulation are explained and study. The measurement method described in this section will be applied in chapter 3 and 4.

2.11.1 Density Distribution

In this simulation, density distribution plays an important role to provide deep understanding of liquid condition in the simulation. In figure 2.10, the density distribution in the simulation system is measure by divide the system into the slab definition in the *z*-direction with an approximate thickness of 0.02Å**.** The density distribution is obtained by count the average number of molecules or atoms in each layer and then divided the average number of molecules to the size of the layer in the unit of volume m^3. Then the local number of density (m^{-3}) is obtained. The local numbers of density then multiply with the molar mass of the molecules and divide by the Avogadro constant. From here density distribution is obtain for the system which in kg/m^{-3} for each layer (Abdul Rafeq bin Saleman , Hari Krishna Chilukoti , Gota Kikugawa , Taku Ohara, 2017).

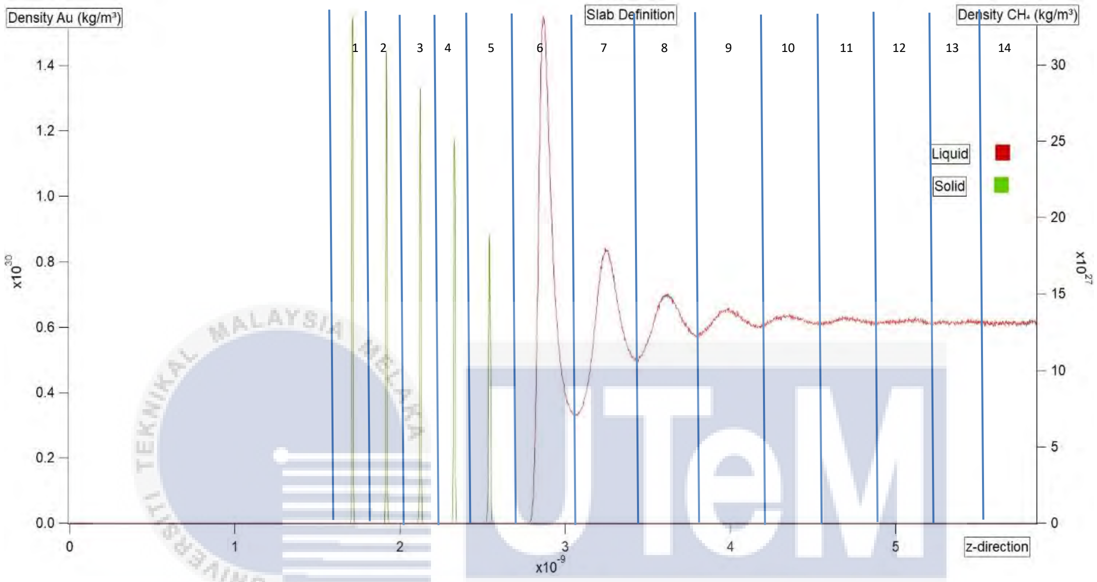

Figure 2.10 Slab Definition

2.11.2 Temperature Distribution

In the simulation, the measurement of temperature distribution in the system is based on the density distribution of the system. Based on the previous author, the density of the liquid film in the simulation must be in the condition of saturated liquid which at the temperature of 0.7 T_c. Whereby T_c is the critical temperature for the saturated liquid. The temperature in the system shows the temperature keeps decrease as the temperature flow from left to right. In the system, there exists a temperature jump (TJ) at the S-L interface which shows temperature discontinuity or temperature drop as the heat flow through the interface. TJ exists in the system is causes by the AMM and DMM which is the phonon mismatch or scattering at the interface. Normally the TJ occurs between the solid and liquid contacting layer where the temperature difference or temperature drop happen. From there, the TJ is determined.

2.11.3 Heat Flux Measurement

Irving and Kirkwood are first to derived the heat flux vector in molecular dynamic by modifying the expression under the assumption of constant system with non-macroscopic fluid flow (J.H.Irving, 1950). From here, instantaneous heat flux is achieved. The equation (5.5) is used to measure the average heat flux across the direction of heat flux. The equation (5.5) is the equation of heat flux J_x under a control volume V.

$$J_x V = \sum_{s}^{N} V_{x,s} E_s` + \sum_{n-body\ potential} \sum_{s_1} \sum_{s_2 > s_1} \dots \sum_{s_n > s_{n-1}} [\frac{1}{n} \sum_{\alpha=1}^{n-1} \sum_{\beta=\alpha+1}^{n} (F_{s_{\alpha,U}} \times v_{s_\alpha} - F_{s_\beta,U})(x_{s_\alpha} - x_{s_\beta}) * \tag{5.5}$$

In equation (5.5), the term $V_{x,s}$ represent as velocities of site s in a x-direction and E_s refer as internal energy in site s. $F_{s_\alpha,U}$ term is the force acting on site s_α while v_{s_α}term is the velocity vector on site s_α. The distance of x-direction between the site s_α. and s_β is represent as $(x_{s_\alpha} - x_{s_\beta})$ in equation (5.5) under control volume. From the equation (5.5), it can be separated into two terms. The first term refers as internal energy from the kinetic and potential of the particle while the second term refers as the force of the intermolecular interaction between particles and the total of all the n-body potential. At here, there are two methods that used to collect the data of the heat flux. The method which is the heat flux is based on the control surface and the heat flux equation is divided into three degrees of freedom based on the motion of the particles.

As for heat flux across control surface method, it measures the heat flux under control surface. The equation (5.6) represents the heat flux J_x across control surface S_{cs}.

$$J_x S_{cs} = \sum_{s} [\, E_s/1] \frac{v_{x.s}}{[v_{x,s}]} + \sum_{n-body\, potential} \sum_{s_1} \sum_{s_2 > s_1} \cdots$$

$$\cdot\cdot \sum_{s_n > s_{n-1}} [\frac{1}{n} \sum_{\alpha=1}^{n-1} \sum_{\beta=\alpha+1}^{n} (F_{s_\alpha} \times v_{s_\alpha} - F_{s_{\beta,U}} \times v_{s_\beta}).\{H(x_{s_\alpha} - x_{c_s}) - H\left(x_{s_\beta} - x_{c_s}\right)\} \tag{5.6}$$

In equation (5.6), the terms for $(/1)$ refer as the value per unit time, x_{cs} is the position of the control surface in *x*-direction. Meanwhile H is the Heaviside step function. The Heaviside step function is given in equation (5.7):

$$H = \begin{Bmatrix} 0 & (x < 0) \\ 1 & (x > 0) \end{Bmatrix} \tag{5.7}$$

As for the heat flux equation of three degree of freedom (DOF), this heat flux is based on the motion of the particle. The transfer of energy in particle only exists when the particle is in motion. Equation (5.8) is the rate of kinetic energy.

$$\dot{E}_i^{\,kinetic} = \sum_j F_{ij} \times v_i \tag{5.8}$$

In equation (5.8), the term $\dot{E}_i^{\,kinetic}$ is the rate of kinetic energy of particle i. For the term F_{ij} refer as the force acting on particle i from the contribution of all other particles j. v_i is the velocity vector of particle i in equation (5.8). Furthermore, the $F_{ij} \times v_i$ can be decomposed into three direction which is in (*x, y, z*) direction. $F_{ij} \times v_i$ is decomposed because the particle is in inter-particles force and translational motion. The decomposed $F_{ij} \times v_i$ is represented in equation (5.9):

$$F_{ij} \times v_i = F_{ij,x} \times v_{i,x} + F_{ij,y} \times v_{i,y} + F_{ij,z} \times v_{i,z} \tag{5.9}$$

In equation (5.9), the term of $F_{ij,x}$ is the intermolecular force acting between the particle i and j in the x-direction while $v_{i,x}$ is the velocity of particle i in x-direction. The terms $F_{ij,y}$, $F_{ij,z}$, $v_{i,y}$, $v_{i,z}$ is same as above but different in direction.

2.12 Conclusion

In conclusion, the measurement method for the density distribution, temperature distribution and heat flux are studies. Next, the fundamental of MD simulation are analyse in order to get the general ideas about the MD simulation. Lastly, the relevant detail about the pass studies of thermal rectification and the potential function used to model the solid and liquid model are examined.

CHAPTER III

METHODOLOGY

3.1 Introduction

Methodology is one of the parts of a studies where all the action and activity is list out and arrange in a systematic method. In this chapter, the methodology of the research flow and the simulation used to complete the studies are described. The procedures and steps used to complete the objective mentioned are explained in this chapter.

3.2 Simulation Model & Potential Function

In molecular dynamic simulation, the solid and liquid in the system are replicated by the atoms or molecules and potential functions. The potential functions in the simulation system are referred here as the interaction between atoms or molecules.

3.3 Simulation Model

In the present system, the model is set at which the liquid methane (CH_4) is confined between the two parallel solid gold (Au) walls by using molecular dynamic simulation (MD) which is shown in figure 3.1. Liquid confined between two parallel solid walls have been utilized in a number of applications to investigate interfacial thermal resistance (Abdul Rafeq bin Saleman , Hari Krishna Chilukoti , Gota Kikugawa , Taku Ohara, 2017) (S.Murad, I.K.Puri, 2012) . Therefore, this study utilized the model. The size of simulation box, number of solid atoms in x, y and z-direction and the number of liquid molecules (CH_4) is tabulated in table 3.1 for the cases of (100), (110) and (111) crystal planes. In this simulation model, liquid methane (CH_4) is chosen as the liquid model while gold (Au) is used as the solid wall. The three types of FCC crystal planes of (100), (110), and (111) are used on the both sides (left and right side) of the two solid walls which contact with the liquid methane (CH_4) throughout the simulations. In this simulation as to ensure that the simulation model does not drift, a fixed boundary condition of the outermost layer of the solid atom is set in the *z*-direction for both solid walls and the periodic boundary condition is set in the *x* and *y*-direction in the simulation system. In the simulation model, the S-L interfaces is referred as the location where the liquid and solid is in contact with each other.

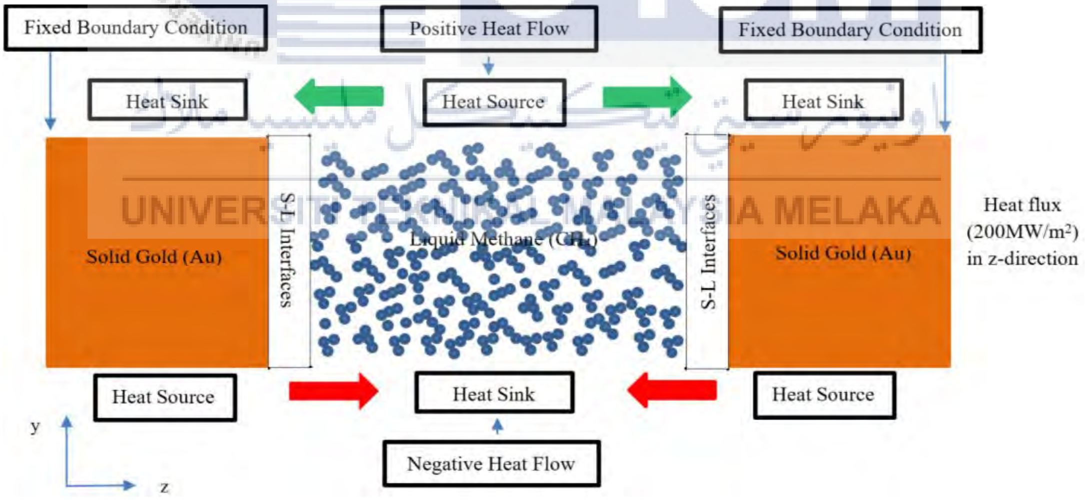

Figure 3.1 Outline of simulation condition

Table 3.1 Species of liquid alkane, types of crystal plane, size of simulation box, number of molecules for liquid methane and number of solid atoms in *x*, *y* and *z* axis

Species of liquid alkane	Types of crystal plane	Size of simulation box $L_x \times L_y \times L_z$ $(\dot{A})$	Number of molecules for liquid methane (CH_4)	Number of solid atoms in *x*, *y* and *z* axis
CH_4	(100)	41 x 41 x 118	2795	10 x 20 x 6
	(110)	47 x 49 x 119	3896	16 x 12 x 10
	(111)	41 x 40 x 119	2773	14 x 16 x 6

3.4 Solid of Gold (Au)

In the simulation system, gold (Au) is chosen as the two solid walls in the simulation system. Gold (Au) was chosen as the two parallel solid walls because gold have the basic crystal structure and most of materials consists of crystal structure. As such, gold (Au) is suitable candidates to studies the characteristic of surface structure in the simulation system. The solid of gold (Au) contacting liquid film system gives general information related to the characteristic of thermal energy transfer at the S-L interface and gold (Au) believed to has the lattice structure of face-centered cubic (FCC). The crystallographic direction is defined as the direction of the cross section of the lattice**.** In crystallographic direction, the (100), (110), and (111) crystal plane are the three common direction for FCC. Figure 3.2 shows the surface structure of solid wall in contact with liquid where the Figure 3.2 (a) represent (100) crystal plane, figure 3.2 (b) represent (110) crystal plane and figure 3.2 (c) represent (111) crystal plane. The 0 indicating the origin of the coordinate.

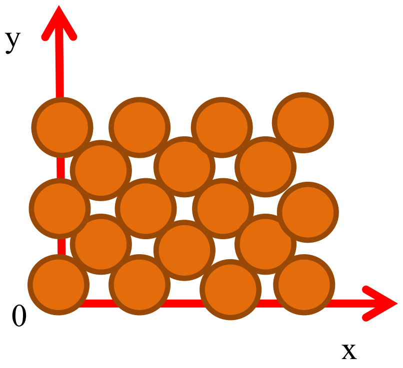

a) (100) crystal plane

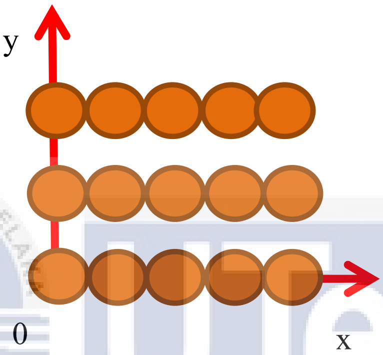

b) (110) crystal plane

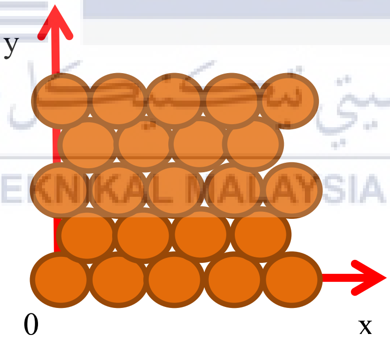

c) (111) crystal plane

Figure 3.2 Surface of structure of (100), (110), and (111) crystal plane

For the case for this simulation, Morse potential is selected to modelled the solid walls. The Morse potential was selected since it has the simple potential functions, as such the computation time can be reduced. In addition, Morse potentials have been used in a number of publications (G. Kikugawa , T. Ohara, T. Kawaguchi, E. Torigie, Y. Hagiwara, Y. Matsumoto, 2009) (A.R. bin Saleman, H.K. Chilukoti, G. Kikugawa, M.Shibahara, T.Ohara, 2017) and the results have close approximation to the experimental results. The Morse potential function is given in equation (6.0).

$$\Phi\left(r_{ij}\right) = D_e\ [e^{-2\alpha\,(r_y - r_u)} - 2e^{\alpha(r_y - r_u)}] \tag{6.0}$$

$$\alpha = \sqrt{\frac{K\ e}{2D}} \tag{6.1}$$

In equation (6.0), the terms $\Phi\left(r_{ij}\right)$ is represent as the interaction energy between the atom i and j which is separated by the distance r_{ij}. Meanwhile the term D_e in equation (6.0) represent as the well depth that defined the relative to the separated atoms. r_y is the coordinate perpendicular to the surface and r_u is the equilibrium bond distance. The parameter of gold for D_e is $7.6148\ \times 10^{-20} J$, r_u is $3.0242\dot{A}$ and α is $1.5380\ \dot{A}^{-1}$. α is obtained by using the equation (6.1).The term α represent as width control of the potential and K_e is the force constant at the minimum of the well (Huffaker, 1975) (Definition of Morse Potential, 2017).

3.5 Liquid Methane (CH_4)

In this simulation system, liquid methane (CH_4) is chosen as the liquid model. The uses of liquid methane (CH_4) in simulation system provide a better understanding of the characteristic of thermal energy transfer in liquid. Liquid methane (CH_4) have been utilized here since it have been applied in many engineering applications (Balaji, 2017). In this study the Lennard-Jones (LJ) 12-6 potential is used to modelled the liquid methane (CH_4). The LJ 12-6 is given as follows:

$$U^{LJ}\left(r_{ij}\right) = 4\varepsilon_{ij}[(\frac{\sigma_{ij}}{r_{ij}})^{12} - (\frac{\sigma_{ij}}{r_{ij}})^{6}] \tag{6.2}$$

The U^{LJ} is referred as intermolecular interaction between atom i and j. r_{ij} is referred as the distance between atom i and j. The first term of equation (6.2) is referred as the repulsive interaction while the second term is represent the smoother attractive interaction. The ε_{ij} is the energy between atoms i and j while σ_{ij} is the size parameter of molecules between atoms i and j. The parameters for the interaction is based on the Transferable Potential for Phase Equilibria (TraPPE) force field, where the value of ε_{CH_4} is $2.0433 \times 10^{-21} J$ while the value of σ_{CH_4} is $3.73 \dot{A}$ (M.G. Martin, J.I. Siepmann, 1998) (B.L. Eggimann, 2007). The TraPPE parameter have been utilized here since the interaction force in closely replicated the actual liquid as reported in past studies (A.R. bin Saleman, H.K. Chilukoti, G. Kikugawa, M.Shibahara, T.Ohara, 2017) .

3.6 Simulation condition

The time integration of the simulation is perform by using reversible reference system propaganda algorithm (r-RESPA) (M.E. Tuckerman, 1992) . For the case of this simulation system, 1fs is set to measure for the molecular interaction forces. Initially, the temperature of the simulation system is raised slowly to the targeted temperature which at the 0.7 T_c of liquid (CH_4). Here T_c is the critical temperature of the liquid methane (CH_4). The value of the 0.7 Tc of the liquid methane (CH_4) is tabulated in table 3.2 which is reported by Torii et al (Taku Ohara, 2011). The temperature in the system is set at the 0.7 T_c is to ensure the liquid methane CH_4 is in the liquid state. Then the temperature of the simulation system is maintained at the targeted temperature until a uniform temperature is acquired throughout the simulation system for 1 to 3 million-time steps. Then, the two opposite heat flow is applied across the simulation system at the heat source and heat sink for 4 to 8 million time steps until steady state is acquired. Here for negative heat flow direction, the solid wall is act as a heat source and the liquid is act as a heat sink at which the heat flow from solid to liquid and the opposite referred to as the positive heat flow direction. The position of the heat source and heat sink is as shown in Figure 3.1. A constant heat flux of 200 MW/m^2 is applied for the present simulation system. In order to generate a constant heat flux, the temperature control was set up in the control region for both sides of the solid wall and at the center in the liquid region by using velocity scaling method. In liquid region, the temperature control is set at the center of the system with the width of 0.02 $\dot{A}$, while at the solid region the width is approximately 0.01 $\mathring{A}$ on both sides of the solid walls. The temperature control was set to ensure that the temperature of the adsorption layer of the liquid molecules near the S-L interface is the same for both cases of the positive and negative heat flow directions and the types of crystal plane contacting the liquid. At a steady-state, a temperature jump (TJ) or temperature discontinuity is shown at the S-L interface on the left and right side that in the simulation system for the case of positive and negative heat flow. The TJ will be evaluated in the next chapter. Then after steady state is acquired, the data acquisition run is set to collect the heat flux data across the simulation system for 10 to 20 million-time steps. The variation in the number of time step is to make sure the data converged that is related to the number of molecules present in one simulation model.

Table 3.2 Critical temperature T_c, triple point temperature, average temperature and the temperature setup for the species of liquid alkane (Taku Ohara, Tan Chia Yuan, Daichi Torii, Gota Kikugawa and Naohiro Kosugi, 2011)

Species of liquid alkane	Critical temperature T_c (K)	Triple point temperature (K)	Average Temperature (K)	Heat Sources T_H (K)	Heat Sink T_L (K)
CH_4	190.00	90.70	133	200	100

3.7 Validation of the simulation systems

In order to validate the simulation system, the density distributions of the liquid CH_4 in the present system, is measured. The simulation system is first divided into slab definition in the z-direction with the thickness of 0.02 Å as shown in the chapter 2 in figure 2.10. The number of liquid methane (CH_4) molecules in each layer is counted for each time step. Then, the number of liquid molecules in each layer is averaged throughout the time steps. Such methods, is referred as ensemble average. Next, the value of the ensemble average is divided to the size of simulation box in m^3 which is referred here as local density. Then the local density of liquid methane (CH_4) is multiply with the molar mass of the liquid methane (CH_4) and then divided by Avogadro number. The value obtains for the density distribution of liquid methane (CH_4) in the present simulation is compare to the actual density distribution of the liquid methane (CH_4). The sample calculation of density distribution for the crystal plane (100) is presented in the appendices.

CHAPTER IV

RESULT AND DISCUSSION

4.1 Introduction

In this chapter, the result of the temperature distribution, density distribution and temperature jump (TJ) for (100, 110, 111) crystal planes will be elaborates in order to understand the influence of surface structure of solid on the thermal rectification at S-L interfaces. The density distribution is calculated by divided the simulation system into slabs with a thickness of 0.02 Å in the *z*-direction and the average number of molecules in each slab is counted. Then, the average number of molecules in each slab is divided by the size of the slab to obtain the local density (m^{-3}). From the local density, the local density is divided by Avogadro number to get the density distribution (kg/m^3) for each slab. As for the temperature distribution of the system, the temperature of the system is measured by using the slab definition. As such, the divided slab definition for measuring the temperature distribution is based on the density distribution. The calculation for the temperature distribution is based on the kinetic energy correspond to the random velocity of the molecules.

In section 4.1, it shows the positive and negative heat flow of the density distribution for the crystal plane (100). From here, the influence of the heat flow direction on the density distribution of CH_4 is discussed and the behaviour of the first adsorption layer of the liquid molecules at the S-L interface is elaborated in term of packing density. As for the solid region, the layer of peak height for the crystal plane (100) is describe in this section.

In section 4.2, it shows the comparison of positive heat flow of density distribution for the crystal plane (100, 110, 111). From here, the gap distance and the height of the first adsorption layer for the crystal plane (100, 110, 111) is discussed in this section. As for the solid region, the layer of peak height for the crystal plane (100, 110, 111) is compared and elaborated.

In section 4.3, the result shows the positive heat flow of the temperature distribution for the crystal plane (100, 110, 111). In this section, the TJ for the crystal plane (100, 110, 111) is compare and discussed. The surfaces structures of the crystal plane (100, 110, 111) is elaborated.

In section 4.4, the result shows the comparison between the positive and negative heat flow for the crystal plane (100). The influence of the positive and negative heat flow for the temperature distribution is discussed and the TJ for the positive and negative heat flow is described.

In section 4.5, the average TJ of the positive and negative heat flow for the crystal plane (100, 110, 111) is tabulated in the table x in order to analyse and see the difference of TJ between the positive and negative heat flow for the crystal plane (100, 110, 111).

In section 4.6, the results show the TBR for the crystal plane (100, 110, 111) of the positive and negative heat flow. The TBR result for each of the crystal plane is tabulated in the table 4.1 in order to provide a clear understanding about the characteristic of the types of crystal planes that influence the TBR at the S-L interfaces.

In section 4.7, the TBC for the crystal plane (100, 110, 111) is tabulated in table 4.2 and the characteristic of the crystal plane that influenced the TBC at the S-L interfaces are explained. In this section, the heat flux is decomposed based on the molecular motion of the *x*, *y* and *z*-component in order to observe the heat flux transfer by each of the component in the crystal plane. The total heat flux against the average TJ for the crystal plane (100, 110, 111) is shows in this section in order to clarify the deviation in TBC between the positive and negative heat flow.

In section 4.8, the TRR result is tabulated in table 4.3 in order to verify the thermal rectification for the crystal plane (100, 110, 111). The TRR for the crystal plane (100, 110, 111) is compare and discuss in this section.

4.2 Density Distribution (100)

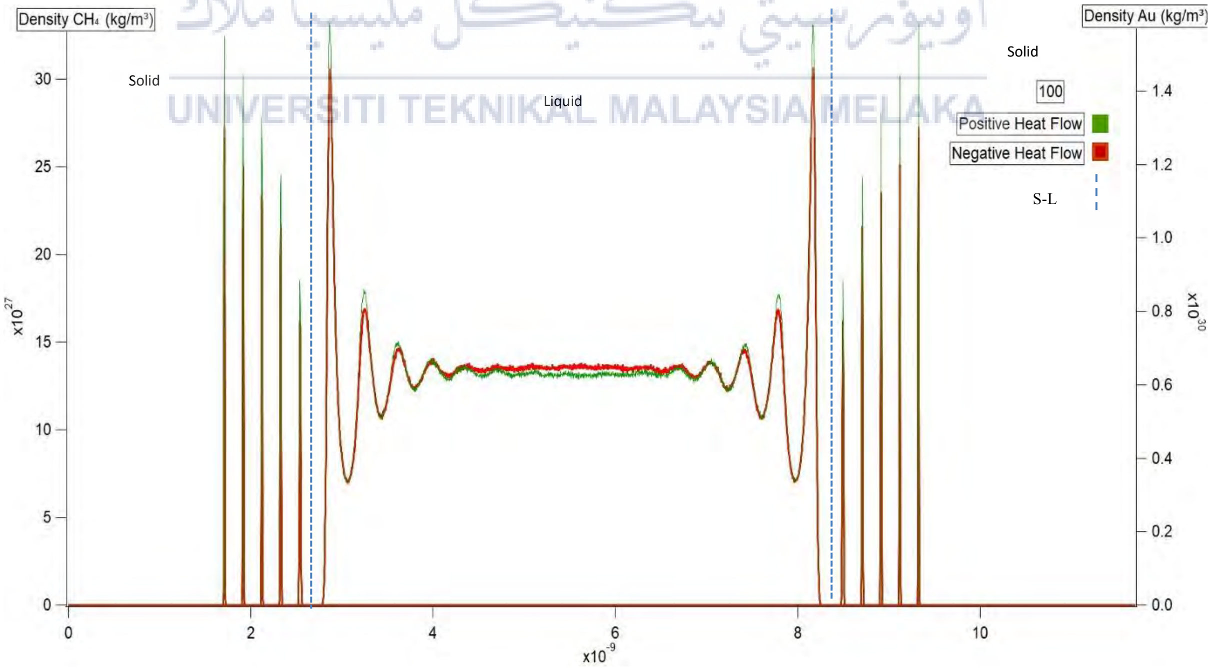

Figure 4.1 Density Distribution (100)

From the graph in figure 4.1, the packing density of the first adsorption layer for the positive heat flow is higher compare to the packing density for the negative heat flow. It is because in the case of positive heat flow, the lower temperature of the solid wall at the S-L interfaces causes the liquid molecules easily to absorb into the crystal plane. Therefore, causes the first adsorption layer of the positive heat flow to be higher packing density compare to the first adsorption layer for the case of negative heat flow. For the flat distribution, the negative heat flow seems to be higher packing density compare to the positive heat flow because the temperature of the negative heat flow is lower than the temperature of the positive heat flow at the flat distribution. It is because the higher temperature causes the liquid molecules to move significantly hence result in lower density. From here, the temperature is one of the factors that can influence the packing density of the liquid molecules and solid atom. Where high temperature generates lower packing density. At the solid region, the peak height of the layer of the solid atom for the positive heat flow is higher compare to the peak height of the solid atom for the negative heat flow. One of the reasons which is the temperature of the solid wall for the case of the positive heat flow is lower compare to the case of the negative heat flow. Hence, result in higher peak height of solid atom for the case of the positive heat flow than the case of negative heat flow.

4.3 Density Distribution (100, 110, 111)

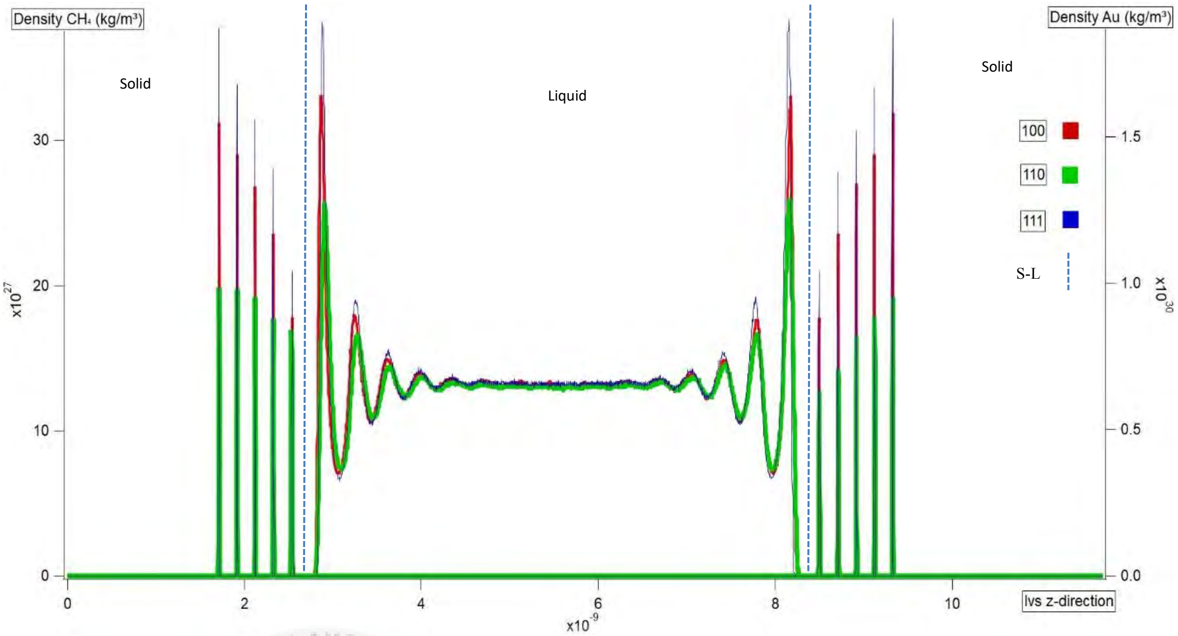

Figure 4.2 Density Distribution (100, 110, 111)

From the graph in figure 4.2, the region of temperature control of the liquid CH_4 is act as a heat source while the region of the temperature control of the solid Au is act as a heat sink. As such, the temperature of the solid Au is lower than the temperature of the liquid CH_4. At the solid region, the layers with the peak at the end of the simulation system are refer as the layer of the solid atom arranged on its lattice position. The layer of peak height of the solid Au is getting lower when it come toward the S-L interfaces for the case of (100, 110 and 111). The highest layer of peak height of the solid Au is the crystal plane (111) follow by the crystal plane (100) and (110). As for the liquid region, the density distribution of the liquid CH_4 tend to oscillates to form a first adsorption layer at the S-L interfaces and tend to disappear as it moved toward the centre of the simulation system. To compare the different in first adsorption layer, the crystal plane (111) has the highest first adsorption layer follows by the crystal plane (100) and (110). This is because the higher layer of peak height of the crystal plane (111) tend to generate higher packing density which cause the first adsorption layer for the crystal plane (111) to increase. Other than that, there exists a different in gap distance for the crystal plane (110). One of the reasons which is the crystal plane (110) have an asymmetric arrangement surface structure between the *x*-axis and *y*-axis which create a corrugation in the lattice-scale on the surface of the crystal plane (110). Therefore, the liquid molecules at the S-L interfaces are easily absorbed into corrugation which result in change to the gap distance.

4.4 Temperature Distribution (100, 110, 111)

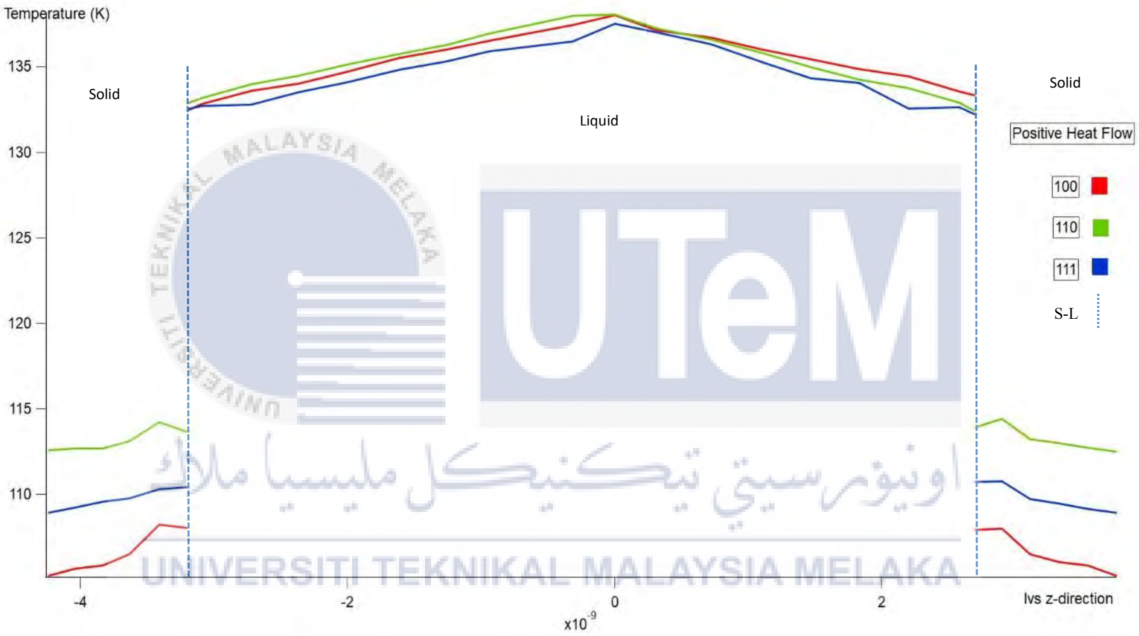

Figure 4.3 Temperature Distribution (100,110,111)

From the graph in figure 4.3, it is found that the temperature for the first adsorption layer are approximate the same temperature which is at 133K for crystal plane (100, 110 ,111). The crystal plane (110) has the smallest temperature jump as compare to crystal plane (100) and (111). One of the reasons that is the crystal plane (110) has an asymmetric crystal plane and lattice-scale corrugation. The liquid molecules near the S-L interface are absorbed into the lattice scale corrugation thus increasing the chance of intermolecular interaction between solid and liquid. From here this cause the thermal boundary conductance (TBC) to increase thus result in smaller TJ. But as for the crystal plane (100) and (111), both of this crystal plane does not have significant lattice-scale corrugation but both of the crystal plane has a symmetry crystal plane. By referring the graph, the reason which cause the TJ for the crystal plane (100) and (111) to be differ which is the number of solid Au atom which present at the S-L interfaces. The number of solid Au atom for the crystal plane (100) are lesser compare to the crystal plane (111). Therefore, this cause the TJ for the crystal plane (100) to has higher TJ compare to the crystal plane (111).

4.5 Temperature Distribution (100) (Positive and Negative Heat Flow)

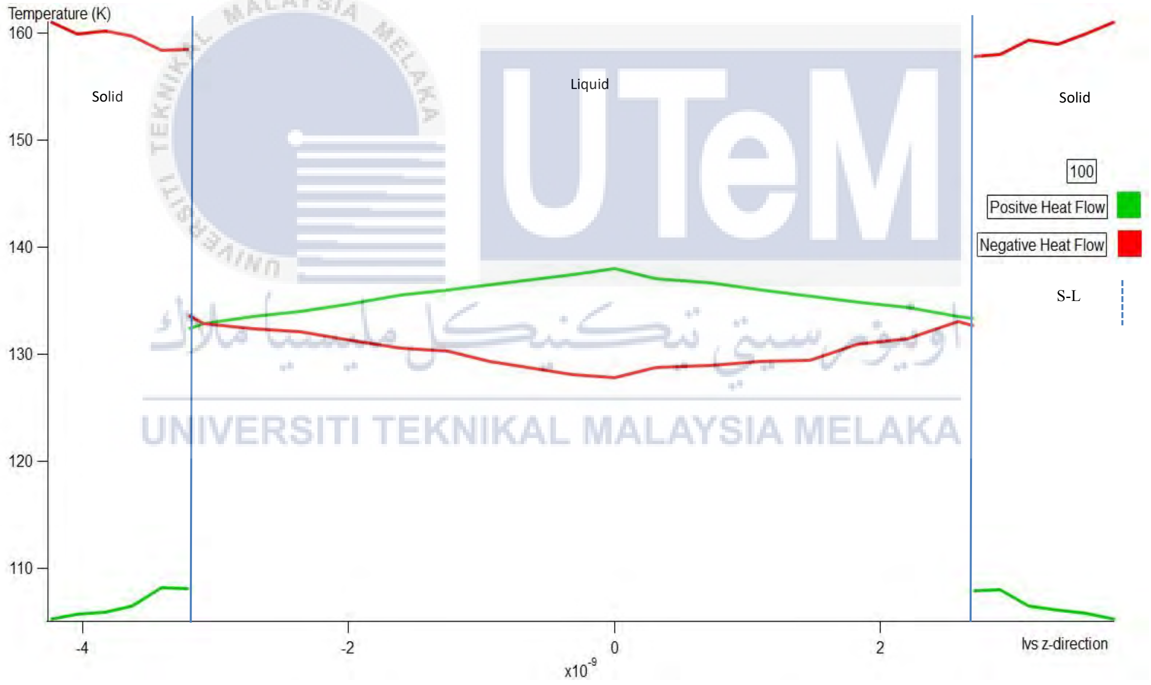

Figure 4.4 Temperature Distribution (100) (Positive & Negative heat flow)

From the figure 4.4 above, it shows the temperature distribution for the crystal plane (100) for the positive and negative heat flow. The green line represents as the positive heat flow while the red line represents as the negative heat flow. The temperature of the system is calculated based on the kinetic energy corresponding to the random velocity of the molecules. From here, the temperature of the first adsorption layer are approximate the same at 133K for both positive and negative heat flow. At the S-L interface, there exists a TJ at both side of the system. It seems like the TJ for the negative heat flow is larger than the temperature jumps for the positive heat flow for the crystal plane (100). It is because the temperature of the solid for the positive heat flow is lower than the temperature of the solid for the negative heat flow.

4.6 Temperature Jump (TJ)

Table 4.1 Average temperature Jump (TJ) (100, 110, 111)

Crystal Plane	Direction of Heat Flow	Average Temperature Jump (K)
(100)	Positive	25.08
	Negative	25.73
(110)	Positive	18.72
	Negative	21.00
(111)	Positive	22.15
	Negative	24.21

Based on the result shown in the table 4.1, the TJ for the crystal plane (100, 110, 111) is calculated by taking the average TJ of the both side of the simulation system. To measure the TJ, the TJ is measured at the temperature of the liquid and solid which is fitted to the straight line and then extrapolated to the midpoint between the solid and liquid contacting layers where the temperature difference between solid and liquid is determined. From the result obtain in the table 4.1, there are a different in TJ between the positive and negati11ve heat flow for the crystal plane (100, 110, 111). The difference in TJ is shows the existence of the thermal rectification at the S-L interfaces. By referring the table 4.1, the TJ for the positive heat flow is lower compare to the negative heat flow regardless of the types of the crystal plane. Next, the TJ for the crystal plane (110) is much larger compare to the crystal plane (100). One of the factors that cause the TJ for the crystal plane (110) to be larger which is due to the asymmetric surface structure between the *x*-axis and *y*-axis of the crystal plane (110). The asymmetric surface structure causes the liquid molecules at the S-L interfaces easily to absorbed into the lattice corrugation thus increase the chance of molecular interaction between the solid and liquid and result in large difference of TJ between the positive and negative heat flow for the crystal plane (110). Meanwhile, the TJ between the positive and negative heat flow for the crystal plane (100) is slightly the same because the crystal plane (100) have no significant lattice scale corrugation between the *x*-axis and *y*-axis thus no activation thermal energy transfer. So, this cause the crystal plane (100) have slightly the same TJ between the positive and negative heat flow. As for the crystal plane (111), the TJ for the positive heat flow is 22.15 K and for the TJ for the negative heat flow is 24.45K. Since the crystal plane (100) and (111) have no significant lattice scale corrugation but the TJ for the crystal plane (111) are higher compare to the crystal plane (100). As a hypothesis, the reason at which the crystal plane (111) has higher TJ compare to crystal plane (100) is due to the number of solid atoms that present at the S-L interfaces. Since the number of solid atoms that are present at the S-L interfaces are different between the cases for crystal plane (100) and (111). As overall, the crystal plane (110) has the highest TJ follow by the crystal plane (111) and (100), starting from highest to lowest.

4.7 Thermal Boundary Resistance (TBR)

Table 4.2 Temperature jump, Thermal Boundary Resistance and Heat Flux at the S-L interfaces.

Liquid Alkanes	Crystal Plane	Direction Heat Flow	Heat Flux (MW/m^2)	Average Temperature Jump (K)	Thermal Boundary Resistance (TBR) x 10^{-6} (m^2K/W)
CH_4	(100)	Positive Heat Flow	196.59	24.93	0.1268
		Negative Heat Flow	200.83	25.99	0.1294
	(110)	Positive Heat Flow	199.80	19.30	0.0966
		Negative Heat Flow	200.28	21.73	0.1085
	(111)	Positive Heat Flow	198.81	21.84	0.1098
		Negative Heat Flow	199.20	22.48	0.1126

The thermal boundary resistance (TBR) is measure at which the TJ is inversely proportional to the heat flux in the z-direction. The TBR equation is shown in the equation (6.3) below:

$$TBR = \frac{TJ}{J_z} \tag{6.3}$$

Where the term TJ refer as the temperature jump at the S-L interfaces while the term J_z refer as the heat flux measure across the z-direction. In table 4.2, it shows the data of the heat flux, TJ and TBR based on the direction of heat flow for the liquid methane (CH_4). The larger the value of TJ at the S-L interface and the smaller the value of heat flux cause the TBR to increase in value.

Based on the table 4.2, it is found that the crystal plane (110) has the smallest TBR compare to the crystal plane (100) and (111). One of the factors that cause the crystal plane (110) to have the smallest TBR which is there exists a gap distance in the crystal plane (110). From here, it shows that the gap distance has an influence on the TBR. As for the crystal plane (100) and (111), the crystal plane (111) has smaller TBR compare to crystal plane (100). To make a comparison, the peak height of the surface structure is observed. By referring the result obtained, the peak height of the surface structure for the crystal plane (111) is higher compare to the crystal plane (100). As such, the TBR for the crystal plane (111) is lower compare to the crystal plane (100). This indicate that the higher the peak height of the surface structure will generate higher thermal energy transfer and result in lower TBR at the S-L interfaces.

The result suggests that the TBR at the S-L interfaces for the crystal plane (100) and (111) crystal plane is influence by the peak height of the surface structure that is the number of atoms present at the surface structure. Next, a special scenario has been observed for the crystal plane (110) that is the gap distance that influenced on the TBR at the S-L interfaces. As overall, the TBR over the S-L interfaces are influenced by the gap distance and the peak height of the surface structure.

4.8 Thermal Boundary Conductance (TBC)

Table 4.3 Heat Flux, Temperature Jump and Thermal Boundary Conductance (TBC)

Liquid Alkanes	Crystal Plane	Direction Heat Flow	Heat Flux (MW/m^2)				Temperature Jump (K)				Thermal Boundary Conductance (TBC) (MW/m^{2}K)
			x	*y*	*z*	Total	T_x	T_y	T_z	Average	
CH_4	(100)	Positive Heat Flow	12.73	10.83	173.04	196.59	26.97	27.03	20.80	24.93	7.89
		Negative Heat Flow	11.25	12.54	177.04	200.83	27.12	27.56	23.31	25.99	7.73
	(110)	Positive Heat Flow	12.53	47.45	139.82	199.80	20.41	19.11	18.38	19.30	10.35
		Negative Heat Flow	9.78	47.92	142.59	200.28	22.87	21.49	20.81	21.73	9.22
	(111)	Positive Heat Flow	11.23	8.86	178.72	198.81	23.27	23.39	18.53	21.84	9.10
		Negative Heat Flow	10.76	9.76	178.69	199.21	24.04	23.93	20.10	22.69	8.78

Thermal boundary conductance (TBC) is inversely of the thermal boundary resistance (TBR). The equation (6.4) used to calculate the TBC is as below:

$$TBC = \frac{Jz}{TJ} \tag{6.4}$$

In equation (6.4), the term J_z refer as the heat flux measure across the z-direction and TJ terms refer as the temperature jump at the S-L interfaces. The heat flux and the TJ at the S-L interfaces for the both opposite direction heat flow is calculated and tabulated in table 4.3. According to the equation (5.9) shown in chapter 2, the heat flux is decomposed based on the molecular motion of the *x*, *y* and *z*-component. These three components are call as the degree of freedom (DOF) and the TBC is calculated based on these three components. From the table 4.2, there exists a difference of TJ among the cases of the crystal plane (100, 110, 111) although the system is set at the same condition. Based on the result obtained, the crystal plane (110])has the highest TBC value compare to the crystal plane (111) and (100) starting from highest to lowest, regardless of the heat flow direction. The gradient of each line represents as the TBC. Figure 4.5 to 4.8 shows the thermal energy transfer in *x*, *y* and *z*-component against the average temperature jump.

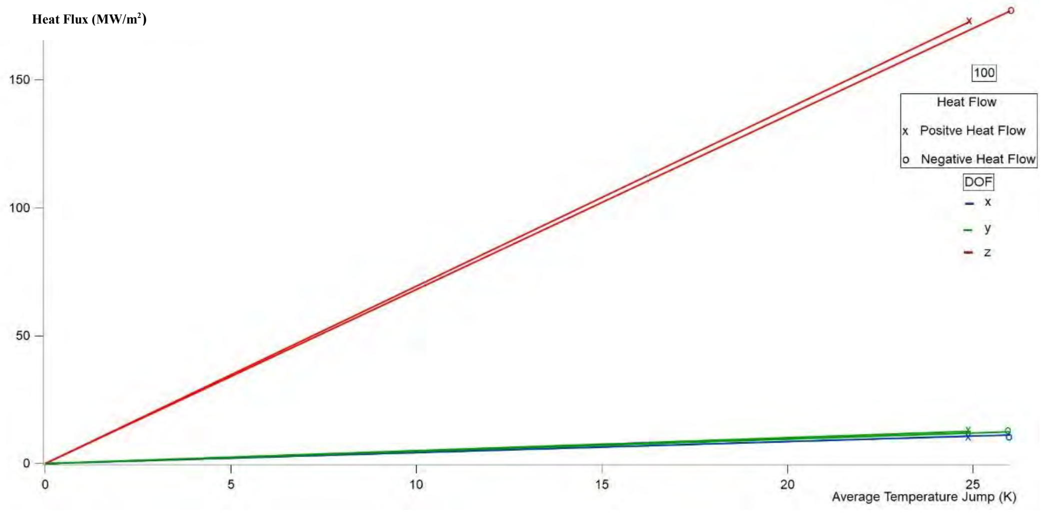

Figure 4.5: Thermal Boundary Conductance (100)

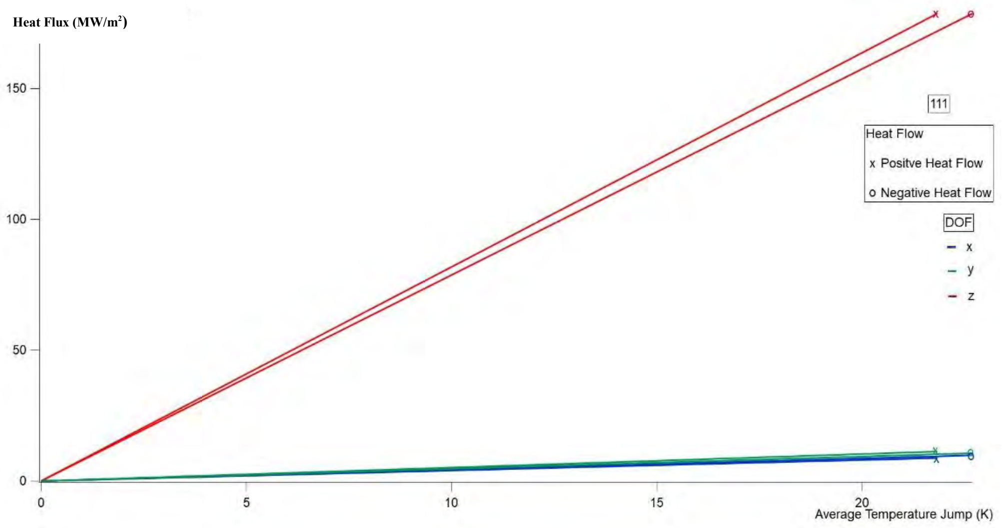

Figure 4.6: Thermal Boundary Conductance (111)

In figure 4.6 above, the blue line represents as the *x*-component, green line as *y*-component and red line as the *z*-component. Based on the figure 4.6, there shows a slight deviation in the z-component while there is no clear deviation in the *x* and *y*-component for the two opposite heat flow. In the case for the crystal plane (100) and (111), most of the TBC is contributed by the *z*-component while *x* and *y*-component do not work much on the TBC. Since there are no lattice scale corrugation at the surface of the crystal plane (100), and (111) so there is no activation of thermal energy for the *x* and *y*-component. This indicate the thermal energy transfer by the *x* and *y*-component are parallel to the interface. From the result obtained, there shows a different in value of TBC for the crystal plane (100) and (111). Since there shows aa difference in the number of solid atoms that present at the S-L interfaces for the case of the crystal plane (100) and (111). The crystal plane (111) seems to have higher TBC compare to crystal plane (100) because the number of solid atoms that present at the S-L interfaces is larger compare to the crystal plane (100), where larger number of solid atoms present at the S-L interfaces generate higher TBC.

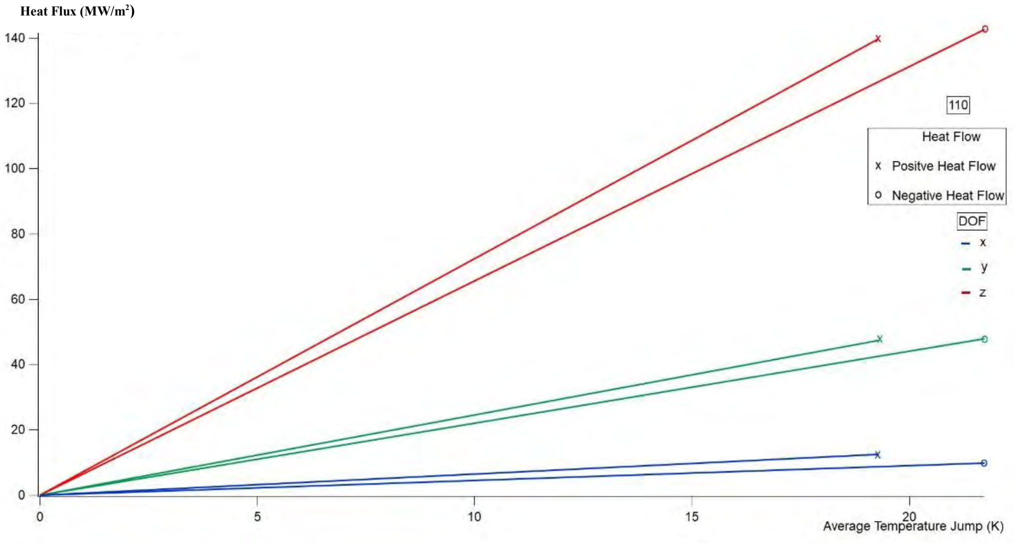

Figure 4.7: Thermal Boundary Conductance (110)

As shown in figure 4.7 above, the deviation between the two opposite heat flow direction is observed for the TBC in *x*, *y* and *z*-component for the crystal plane (110). The TBC in *x*, *y* and *z* shows a slight deviation between the two opposite heat flow. Next, the gradient of *z*-component is higher compare to the gradient of *y* and *x*-component starting from high to low. The TBC for the positive heat flow is higher compare to the negative heat flow. From here, the *z*-component has the higher contribution of TBC follow by *y*-component while the *x*-component do not contribute much to the TBC. One of the factors that cause the *y*-component to work to transfer thermal energy that is due to lattice-scale corrugation that exists on the surface of the crystal plane (110) which causes the liquid molecules near to the S-L interface to absorb into the lattice-scale corrugation. On the other hand, the absorbed liquid molecules increase the chance of molecular interaction between the solid and liquid molecules. Thus, activating the TBC for the crystal plane (110) regardless of the heat flow direction.

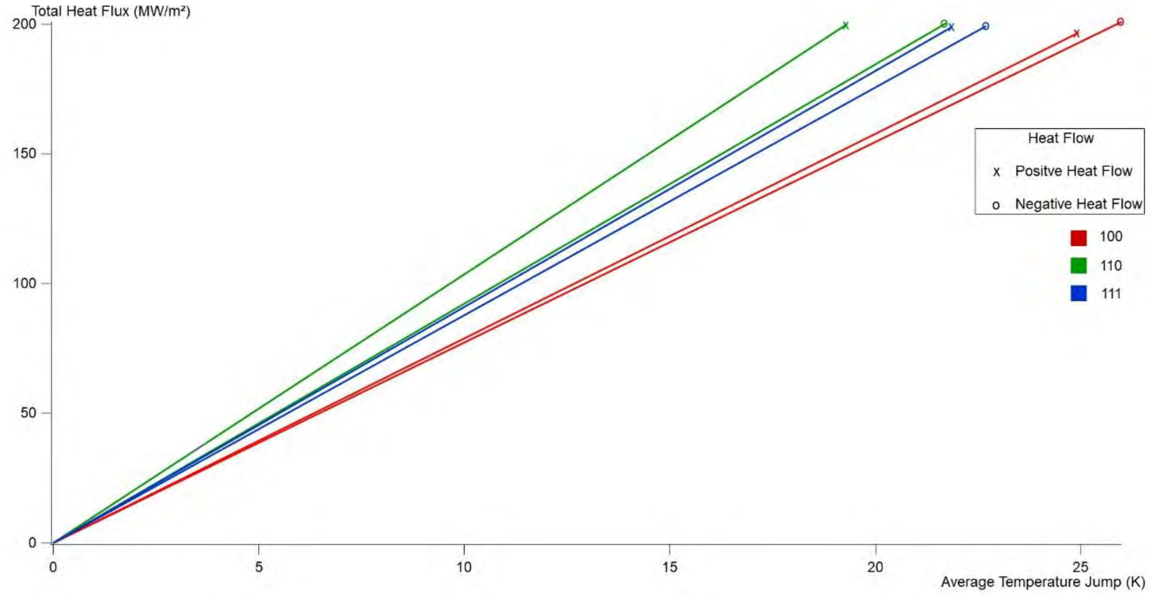

Figure 4.8: Thermal Boundary Conductance (100, 110, 111)

In order to clarify the deviation in TBC between the two opposite heat flow direction, the total heat flux against the average temperature jump for the crystal plane (100, 110) and (111) is plot in one figure 4.8. In the figure 4.8, each of the gradient of the straight line represent as the macroscopic TBC. The red colour gradient represents as crystal plane (100), green colour as crystal plane (111) and blue colour represent as crystal plane (111). As seen in the figure 4.8, the crystal plane (110) has the highest TBC follow by the crystal plane (111) and (100) starting from highest to lowest, regardless of the heat flow direction. In terms of TBC deviation, the crystal plane (110) has the highest deviation follow by crystal plane (111) and (100) starting from highest to lowest, regardless of the heat flow direction. The deviation shown in the figure 4.8 represent as the thermal rectification exists at the S-L interfaces.

4.9 Thermal Rectification Ratio (TRR)

Table 4.4 Thermal rectification for (100,110,111)

Crystal Plane	TBC_P	TBC_N	Thermal Rectification Ratio (TRR) %
(100)	7.89	7.73	2.03
(110)	10.35	9.22	12.29
(111)	9.10	8.78	3.64

In order to achieve the objective of the research, the thermal rectification ratio (TRR) is calculated based on the crystal plane (100, 110, 111). The equation (6.5) is used to calculate the TRR:

$$TRR = \frac{TBC_P - TBC_N}{TBC_N} \times 100\% \qquad (6.5)$$

In equation (6.5), the terms TBC_P and TBC_N refer as the thermal boundary conductance for positive and negative heat flow at the S-L interfaces. The TRR is calculated at which the difference between the TBC_P and TBC_N is divided by the TBC_N. From the table 4.4, the crystal plane (110) has the highest TRR compare to the crystal plane (111) and (100) starting from highest to lowest. The total value of TRR are 12.29%, 3.64% and 2.03% for the crystal plane (110), (111) and (100). From here, it is understood that the lattice-scale corrugation has the highest contribution to the total value of TRR compare to the number of the solid atoms present at the S-L interfaces regardless of the types of the crystal plane.

CHAPTER 5

CONCLUSION

5.1 Conclusion

In this research, the influence of thermal rectification at the S-L interfaces were examined by using MD simulations. In the simulation system, the S-L interfaces are consisting of liquid methane (CH_4) in contact with solid gold (Au) surfaces. The surface of solid gold (Au) is the face-centered cubic (FCC) which consisted of crystal plane (100, 110, 111). According to the first objectives, the influence of thermal rectification effect at the S-L interfaces of a liquid methane (CH_4) in contact with face-centered cubic (FCC) is clarified by using MD simulation. Based on the result obtained, it was found that the crystal plane (110) has the highest thermal rectification compare to crystal plane (111) and (100) as the TBC for the crystal plane (110) shows larger deviation between the positive and negative heat flow compare to crystal plane (111) and (100). Furthermore, the average temperature jumps between the positive and negative heat flow for the crystal plane (110) is higher compare to the crystal plane (111) and (100). From here, the thermal rectification at the S-L interfaces is clarify based on the deviation of TBC and the average TJ between the positive and negative heat flow at the S-L interfaces. As for the second objective, the influences of surface structure of solid on the thermal rectification at S-L interface is clarified by looking into the packing density of solid gold (Au) at the S-L interfaces and the surface structure of the solid at the S-L interfaces. Based on the result obtained, the packing density of the solid golid (Au) surface is influencing the packing density of the first adsorption layer of the liquid methane (CH_4). Where lower packing density of solid (Au) at the S-L interfaces seems to generate lower first adsorption layer of liquid methane (CH_4). Next, the crystal plane (110) has the highest thermal rectification compare to crystal plane (100) and (111) because the crystal plane (110) has the lattice-scale corrugation between the *y*-axis which shown in chapter 3 figure 3.2. The lattice scale corrugation causes the liquid molecules at the S-L interfaces easily to absorb into the surface structure. The absorbed liquid molecules increase the chance of interaction between the liquid and solid molecules thus activating the TBC in the *y*-component in the crystal plane (110). Hence, the crystal plane (110) result in higher of thermal rectification at the S-L interfaces compare to the crystal plane (111) and (100) due to the lattice scale corrugation that exits at the crystal plane (110). From here, the influence of surface structure of solid on the thermal rectification is clarified.

To analyse the influence of the thermal rectification at the S-L interfaces, the comparison result for the density distribution, temperature distribution, temperature jump (TJ), thermal boundary resistance (TBR) and thermal boundary conductance (TBC) is clarify and discussed in order to obtain a clear understanding about the phenomena of thermal rectification at the contacting surfaces. The structural quantities of the liquid (CH_4) near to the S-L interfaces namely density distribution was examined for every simulation test and the measurement of temperature distribution, density distribution and heat flux are explained. To examine the influence of two opposite heat flow direction for crystal plane (100, 110, 111), a liquid methane (CH_4) in contact with solid gold (Au) FCC are used. The two opposite heat flow direction for the crystal plane (100, 110, 111) were discussed and compared to examine the TJ at the S-L interfaces. In TBC, the heat flux is decomposed into *x*, *y* and *z*-component in order to examine the thermal energy transfer by the *x*, *y* and *z*-component.

The main results of this research are listed as follows:

1. The peak height or packing density of the first adsorption layer are influenced by the peak height of the solid atom at the S-L interfaces, where higher peak height of solid atom generates higher first adsorption layer.
2. The TJ for the positive heat flow is lower than the TJ for the negative heat flow for the crystal plane (100, 110, 111).
3. The crystal plane (110) has the highest thermal rectification follow by the crystal plane (111) and (100). One of the reasons which is the crystal plane (110) has the highest thermal rectification is due to the asymmetric surface structure which cause the liquid molecules easily to absorb into the lattice scale corrugation which result in increasing of molecular interaction between the solid and liquid molecules.
4. The first adsorption layer at the S-L interfaces are influenced by the temperature of the solid wall. Where higher temperature of the solid wall generates lower first adsorption layer at the S-L interfaces.
5. The TBC at the S-L interfaces are influence by the number of solid atoms at the S-L interfaces and the lattice-scale corrugation of the solid surfaces. Large number of solid atoms tend to generate lower TBC.
6. The lattice-scale corrugation has the highest contribution to the TRR compare to the number of solid present at the S-L interfaces.
7. The thermal rectification at the S-L interface for a simple liquid is governed by the lattice-scale structure of solid surfaces and the adsorption layer of the liquid. The adsorption layer of the liquid molecules near the S-L interfaces is influenced by the temperature of the solid wall.

The finding in this research provide a better understanding on the thermal rectification at the S-L interface. In general, the present research is looked into the behaviour of thermal rectification at the contacting surfaces between the liquid methane (CH_4) and the solid gold (Au) with the consideration of asymmetrical heat conduction at the S-L interfaces. Based on the present results, it shows that the behaviour of the thermal rectification is depending on the surface structure of the solid wall. From here, the thermal rectification can be control by manipulate the surface structure of the solid wall. By understanding the phenomenon of the thermal rectification at the contacting surfaces, this understanding can be used to improve and optimized the design of industrial application such as the nano-lubrication system that used for the car engine. At the end of this research, the objective of this research is achieved.

REFERENCES

A. Amania, S. M. (2016). A molecular dynamics simulation on the effect of different parameters on thermal resistance of graphene-argon interface. *Molecular simulation*, 1-8.

A.R. bin Saleman, H.K. Chilukoti, G. Kikugawa, M.Shibahara, T.Ohara. (2017). A molecular dynamics study on the thermal transport properties and the structure of the solid-liquid interfaces between face centered cubic (FCC) crystal planes of gold in contact with linear alkanes liquids. *International Journal of Heat and Mass Transfer*, 168-179.

Abdul Rafeq bin Saleman , Hari Krishna Chilukoti , Gota Kikugawa , Taku Ohara. (2017). Thermal rectification effect on solid-liquid interfaces between face centered cubic lattices and a simple liquid.. *Proceeding of the Asian Conference on Thermal Science 2017 ,ACTS*, 2.

Abdul Rafeq bin Saleman, H. C. (n.d.). A molecular dynamics study on the thermal energy transfer and momentum transfer at the solid-liquid interfaces between gold and sheared liquid alkanes. *International Journal Thermal Science*.

AMRIT, J. (6-8 October, 2014). *Jay amrit kaptiza resistance at niobiumsuperfluid He interfaces*. Retrieved 7 April, 2018, from Slide Player: https://www.slideshare.net/thinfilmsworkshop/jay-amrit-kapitza-resistance-at-niobiumsuperfluid-he-interfaces

B.H. Kim, A. T. (2008). Molecular dynamics simulations of thermal resistance at the liquid-solid interface. *Journal Chemistry and Physics*, 174701.

B.L. Eggimann, J. L. (2007). Application of the TraPPE force field to predictomg isothermal pressure-volume curves at high pressure s and high temperature. *International Journal of Thermophysics*, 764-804.

B.Li, L. W. (2004). Rectification of heat flux. *Physical Review Letter*, 93.

Balaji, D. (24 August, 2017). *What are some uses and applications of alkanes?* Retrieved 3 April, 2018, from Quora: https://www.quora.com/What-are-some-uses-and-applications-of-alkanes

Basjes, M. S. (1984). Embedded-atom-methid : Derivation and application to impurites, surface and other defects in metals. *web.mit.edu*, 6443.

Berendsen, H. (24 January, 2014). *Berendsen Baraostat*. Retrieved 1 March, 2018, from SKlogwiki: http://www.sklogwiki.org/SklogWiki/index.php/Berendsen_barostat

Berne, B. J. (1999). Molecular Dynamics in Systems with Multiple. *link springer Ideas Springer-Verlag Berlin Heidelberg 1999*, 306.

C.W. Chang, D. O. (2006). Solid-state thermal rectifier . *Science*, 1121-1124.

Chemistry. (Feb 15, 2015). Retrieved 4 March, 2018, from Chemistry stack exchanger: https://chemistry.stackexchange.com/questions/27331/please-explain-the-following-graph-for-a-quantum-mechanical-harmonic-oscillator

D. Toruu, T. O. (2010). Molecular-scale mechanism of thermal resistance at the solid-liquid interfaces: Influence of interaction parameters between solid and liquid molecules. *Journal Heat Transfer*, 12402.

D.Beeman. (1976). Some multistep methods for use in molecular dynamics calculations. *Science Direct*, 139-139.

D.Beeman. (19 April, 2010). *Beeman's Algorithm*. Retrieved 1 April, 2018, from SklogWiki: http://www.sklogwiki.org/SklogWiki/index.php/Beeman%27s_algorithm

D.Savio, N. ,. (2013). A molecular dynamics study of the transition from ultra-thin film lubrication toward local film breakdown. *Tribology Letters*, 207-220.

Daichi Torii, T. O. (23 October, 2009). *Molecular-Scale Mechanism of Thermal Resistance at the Solid-Liquid Interfaces: Influence of Interaction Parameters Between Solid and Liquid Molecules*. Retrieved 18 March, 2018, from The American Society of Mechanical Engineer: http://heattransfer.asmedigitalcollection.asme.org/article.aspx?articleid=1449794

Definition of Morse Potential. (2017). Retrieved 1 April, 2018, from Chemicool Dictionary: https://www.chemicool.com/definition/morse_potential.html

Democritus. (n.d.). Retrieved 8 March, 2018, from Democritus: http://www.compsoc.man.ac.uk/~lucky/Democritus/Theory/moldyn2.html

Democritus. (n.d.). *Periodic Boundary Condition*. Retrieved 27 February, 2018, from Compsoc: http://www.compsoc.man.ac.uk/~lucky/Democritus/Theory/pbc-mi.html

dmarendu. (2 Feb, 2012). *ph.ed.ac.uk*. Retrieved 1 March, 2018, from Thermostats in Moleclar Dynamic: https://www2.ph.ed.ac.uk/~dmarendu/MVP/MVP03.pdf

Dr. Karina Kubiak, O. (n.d.). *Basic principles of molecular dyanmics (MD) theory*. Retrieved 16 February, 2018, from Archie-West: www.archie-west.ac.uk/wp-content/uploads/2012/06/MD_theory1.pptx

Dror, R. (5 October, 2017). *Web.stanford.edu*. Retrieved 5 March, 2018, from Web.stanford.edu: https://web.stanford.edu/class/cs279/lectures/lecture4.pdf

E. SANZ, C. M. (2013). The properties of fully flexible Lennard-Jones chains in the solid. *Taylor & Francis Group*, 2241-2242.

E.T Swartz, R. P. (1989). Thermal Boundary Resistance. *Review of Modern Physics*, 605-668.

E.V. Kozlov, L. &. (1971). *Calculation of the morse potential for solid gold.* Siberia: Research Gate.

Embedded Atom Method (EAM) Simulation in the MedeA® Environment. (17 February, 2012). Retrieved 4 April, 2018, from Materials Design: http://www.materialsdesign.com/appnote/embedded-atom-method-simulation#fnref:2

G. Kikugawa , T. Ohara, T. Kawaguchi, E. Torigie, Y. Hagiwara, Y. Matsumoto. (2009). A molecular dynamics study on heat transfer characteristics at the interfaces of alkanethiolate self-assembled monolayer and organic solvent. *The Journal of Chemical Physics*.

G.Wu, B. (2007). Thermal rectification in carbon nanotube intramolecular junctions : Molecular dyanamics calculations. *Physical review B*, 085424.

Gilmer, J. B. (1983). Molecular dynamics investigation of the crystal-fluid interface. I. Bulk properties. *Journal Chemistry and Physics*, 79.

Go, D. B. (2010). On the condition for thermal rectification using bulk materials. *Reseach Gate*, 2.

Hoef, M. A. (2000). Free energy of the Lennard-Jones solid. *Journal of Chemical Physics*, 8142.

http://chemistry.umeche.maine.edu/CHY431/MolDyn2.html. (14 January, 2012). Retrieved 28 February, 2018, from http://chemistry.umeche.maine.edu/CHY431/MolDyn2.html:

Huang, L. Z. (n.d.). *A Response Embedded Atom Method of Interatomic Potentials.* Storrs: Arxiv.

Huffaker, J. (1975). Diatomic molecules as perturbed Morse oscillators. I. Energy levels. *Journal of Chemical Physics*, 3175-3180.

J.H.Irving, J. (1950). The statistical mechanical theory of transport processes IV. The equation of hydrodynamics. *Journal of Chemical Physics*, 817.

Jian-Jun Shu, J. B. (2016). A New Model for Temperature Jump at a Fluid-Solid Interface. *Journal Pone*, 1.

K.Puri, S. M. (2012). Communication: Thermal rectification in liquids by manipulating. *THE JOURNAL OF CHEMICAL PHYSICS 137*, 137.

Kieffer. (n.d.). *SlidePlayer*. Retrieved 6 March, 2018, from SlidePlayer: http://slideplayer.com/slide/3448049/

KIMURA, S. M. (1999). A Study on Thermal Resistance over a Solid-Liquid Interface. *Thermal Science & Engineering Vol.7* , 67.

Kofke, R. a. (1995). Thermodynamic and structureal properties of model systems at solid-fluid coexistence. *Molecular Physics*, 85.

L.V.Woodcock. (1971). Isothermal molecular dynamic calculations for liquid salts. *Chemical Physics Letters*, 257-261.

Lang, J. N. (1980). The embedded-atom method: a review of theory and applications. *ScienceDirect*, 2131.

M. Barisik, A. B. (2012). Boundary treatment effects on molecular dynamics simulation of interface thermal resistance. *Journal Computer Physics* , 7881-7892.

M. Hu, J. G. (2009). Thermal rectification at wate/ functionalized silica interfaces. *Applied Physics Letters*, 10-13.

M. Terraneo, M. G. (2002). Controlling the energy flow in non-linear lattices: A model for a thermal rectifier. *Physical Review Letter*, 4302.1-4302.4.

M. Tuckerman, B. B. (1992). Reversible multiple time scale molecular dynamics. *columbia.edu*, 1990.

M.E. Tuckerman, B. G. (1992). Reversible multiple time scale molecular dynamics. *Journal Chemistry Physics*, 1990-2001.

M.G. Martin, J.I. Siepmann. (1998). Transferable potential for phase equilibria. *The Journal of Physical Chemistry*, 2569-2577.

M.S.Shell. (2009). *Advanced molecular dynamics techniques* . Chicago: Engineering.uscb.edu.

Mabraham. (1 September, 2012). *Gromarcs.* Retrieved 6 March, 2018, from Gromarcs: http://www.gromacs.org/Documentation/Terminology/Thermostats

mabraham. (13 Feb, 2013). Periodic Boundary Conditions. *Gromacs*, p. 1.

Maisuria, M. (2013). Effect of Surface Roughness on Heat Transfer. *3rd International Conference on Mechanical, Automotive and Materials Engineering (ICMAME'2013)*, 84.

Molecualr Dynamic. (n.d.). Retrieved 1 March, 2018, from MD Thermostat: http://www.strodel.info/index_files/lecture/MDthermostats_handout.pdf

MS., S. (1898). Ueber warmeleitung in verdunnten gasen. *Amalen der Physik*, 101-130.

My Psdc. (n.d.). Retrieved 13 March, 2018, from My Psdc: http://www.mypsdc.com/item-detail/ic995-1n4760a-electronic-component-diode.html

N.A. Roberts, D. W. (2010). *A Review of Thermal Rectification Observations and Models in Solid.* Nashville, TN USA, 37325: Department of Mechanical Engineering, Vanderbilt University.

Naeem, R. (8 January, 2017). *Chemostry LibreTexts*. Retrieved 4 March, 2018, from Chemostry LibreTexts: https://chem.libretexts.org/Core/Physical_and_Theoretical_Chemistry/Physical_Properties_of_Matter/Atomic_and_Molecular_Properties/Intermolecular_Forces/Specific_Interactions/Lennard-Jones_Potential

Naeem, R. (8 January , 2017). *Lennard-Jones Potential*. Retrieved 4 March, 2018, from Chemistry LibreTexts: https://chem.libretexts.org/Core/Physical_and_Theoretical_Chemistry/Physical_Properties_of_Matter/Atomic_and_Molecular_Properties/Intermolecular_Forces/Specific_Interactions/Lennard-Jones_Potential

Nave, R. (n.d.). *Kinetic Temperature*. Retrieved 27 April, 2018, from Hyperphysics Heat & Thermodynamics: http://hyperphysics.phy-astr.gsu.edu/hbase/Kinetic/kintem.html#c4

Neumann, J. v. (2004). Introduction to molecular dynamics simulation. *John von Neumann Institute for Computing*, 7.

NPTEL. (29 June, 2012). Periodic Boundary Condition PBC. *Module 5 : Introduction to Monte Carlo Methods (Basic Concepts)*, p. 2. Retrieved 27 Feb, 2018, from http://nptel.ac.in/courses/103103036/24

Nuo Yang, G. Z. (2001). *Carbon Nanocone: A Promising Thermal Rectifier.* Singapore ,Science Park II: Department of Physics and Centre for Computational Science and Engineering.

P.Schofield. (1973). Computer simulation studies of the liquid state. *Science Direct*, 17-23.

Pages.drexel.edu. (n.d.). Retrieved 5 March, 2018, from Pages.drexel.edu: http://www.pages.drexel.edu/~cfa22/msim/node36.html

Phillpot, S. (2016 March, 13). *Effect of Microstructure on Thermal Transport Properties of UO2*. Retrieved 7 April, 2018, from Slide Player: http://slideplayer.com/slide/6283170/

Physics 5403: Computational Physics. (- -, -). Retrieved 27 feb, 2018, from web.mst.edu: http://web.mst.edu/~vojtat/class_5403/MolecularDynamics.pdf

Polezhaev, Y. V. (9 February, 2011). Thermopedia. *Thermopedia*, p. 1. Retrieved from Thermopedia: http://www.thermopedia.com/content/1186/

Pollack, G. (1969). Kapitza resistance. *Reviews of Modern Physics*, 48-81.

Puri, S. M. (2012). Thermal rectification in a fluid reservoir. *AIP* , 100.

R.Khare, P. A. (2006). Molecular dynamics simulations of heat and momentum transfer at a solid-fluid interface: relationship between thermal and velocity slip. *International Journal of Heat and Mass Transfer*, 3401-3407.

R.N.Keeler, J. a. (1962). A theoretical consideration of directional effects in heat flow at the interface of dissimilar materials. *International Journal of Heat and Mass Transfer 5*, 967-971.

Raghavan, V. (12 February, 2016). *Research Gate*. Retrieved 5 March, 2018, from Research Gate: https://www.researchgate.net/post/What_is_the_effect_of_temperature_on_thermal_conductivity_of_solids_liquids_and_gases

Rogers, G. (1961). Heat transfer at the interface of dissimilar metals. *Internaltional Journal of Heat and Mass Transfer 2*, 150-154.

Ruhle, V. (2008). *Pressure coupling / barostat.* Journal Club.

S. Murad, I. .. (2012). Thermal rectification in a fluid reservoir. *Applied Physics Letters*, 1-5.

S. Pristic, M. I. (2010). Top Thermal Management Innovations from the Past 100 Years and the Next 100 years. *Panel Session at ITherm2010.* Panel Session at ITherm2010.

S.Corti, M. J. (2013). Molecular dynamic at constant pressure : Allowing the system to control volume fluctuation via a "shell' particle. *Entropy* , 3942.

S.D.Probert, T. T. (1970). Thermal contact resistance: The directional effect and other problem. *International Journal of Heat and Mass Transfer 13*, 789-807.

S.Murad, I. (2014). Dynamic rectification in a thermal diode based on fluid-solid interfaces: constrasting behaviour of soft materials and fluid. *Applied Physics Letters*, 1-3.

S.Murad, I.K.Puri. (2012). Thermal rectification in liquid by manipulating the solid-liquid interfaces. *Journal of Chemical Physics*, 1-4.

Saleman, A. R. (2017). *Structure in liquid of chain in molecules contacting crystal solid surface and molecular scale transfer of thermal energy and momentum over the interface.* Tohoku , Japan: Abdul Rafeq bin Saleman.

Shi, D. L. (25 May, 2016). *SlidePlayer.com.inc*. Retrieved 5 March, 2018, from SlidePlayer.com.inc: http://slideplayer.com/slide/9978512/

Shukla, D. L. (1996). Molecular dynamics and higher-order perturbation-theory results for the anharmonic free energy and equation of state of a Lennard-Jones solid. *Physical Review B*, 54.

Steven J. Stuart, R. Z. (1996). Molecular dynamics with multiple time scales: The selection of efficient. *cs.unc.edu*, 1426.

T. Ohara, D. (2005). Molecular dynamics study of thermal phenomena in an ultrathin liquid film sheared between solid surfaces: The influence of the crystal plane on energy and momentum transfer at solid-liquid interfaces. *Journal Chemistry and Physics*, 214717.

T. Ohara, D. (2010). Intermolecular energy transfer at a solid-liquid interfaces. *Mircroscale Thermophysical Engineering*, 186-196.

T.Ohara, D. (2005). Molecular dynamics study of thermal phenomena in an ultra thin liquid film sheared between solid surface: the influence of the crystal plane on energy and momentum transfer at solid-liquid interfaces. *The Journal of Chemistry Physics*, 214717.

T.Q, V. B. (2015). Interface thermal resistance between liquid water and various metallic surfaces. *Internal Journal Precision Engineer and Manufacturing*, 1341-1346.

T.Q, V. B. (2015). Nano-scale liquid film sherared between strong wetting surfaces: Effects of interface region on the flow. *Journal Mechanics Science and Technology*, 1681-1688.

T.Q, V. B. (2016). Transport phenomena of water in molecular fludic channels. *Scientific Report*, 33881.

Taku Ohara, T. C. (2011). Heat conduction in chain polymer liquids :Molecular dynamics study on the contribution of inter- and intramolecular energy transfer. *Journal of Chemical Physics*, 034507-3 .

Taku Ohara, Tan Chia Yuan, Daichi Torii, Gota Kikugawa and Naohiro Kosugi. (2011). Heat conduction in chain polymer liquid: Molecular dynamics study on the contribution of inter- and intramolecular energy transfer. *The Journal of Chemical Physics 135*, 034507-4.

Teja, T. a. (1996). An Equation of State for Real Fluids Based on the Lennard-Jones Potential. *Journal Physics and Chemistry*, 100.

Termentzidis, S. M. (2012). Thermal conductance at the interface between crystals using equilibrium and. *arXiv*, 11.

Theory of molecular dynaimc simulation. (n.d.). Retrieved 28 February, 2018, from Theory of molecular dynaimc simulation: http://chemistry.umeche.maine.edu/CHY431/MolDyn2.html

Travesset, A. (n.d.). Phase Diagram of Power Law and Lennard-Jones Systems: Crystal Phases. *api.scitation*, 1.

Tuckerman, M. E. (2010). Theory and Molecular Simulation. In M. E. Tuckerman, *Stastiscal Mechanics* (pp. 2-5). New York: Oxford University Press.

Verlet, L. (1967). Computer Experimental on Classical Fluids. *Thermodynamical Properties of Lennard-Jones Molecules*, 98-103.

Vnet Reseach. (n.d.). Retrieved 16 March, 2018, from Thermal transistor: http://www.vet-research.net/item-detail/ic995-1n4760a-electronic-component-diode.html

W.H, T. S. (2007). *The Art of Scientific Computing Third Edition.* New York: Cambridge University Press.

Walker, N. R. (2001). Computational Study of Thermal Rectification. *Computational Study of Thermal Rectification*, 3.

Walker, N. R. (2005). *Computational Study of Thermal Rectification.* Nashville, TN USA, 3732: Department of Mechanical Engineering, Vanderbilt University.

Wegochem. (n.d.). Retrieved 14 March, 2018, from Supplier/Distributor: https://www.wegochem.com/chemicals/lubricant-grease/supplier-distributor

Young, P. (2013). The leapfrog method and ither "sympletic" algorithms for intergrating Newton's laws of motion. *Physics 115/242*, 2.

Zhao, Y. (n.d.). *Math.ucsd.edu*. Retrieved 8 March, 2018, from Brieft introduction to the thermostat: http://www.math.ucsd.edu/~y1zhao/ResearchNotes/ResearchNote007Thermostat.pdf

张戈辉. (2017). *Molecular Dynamics.* China.

APPENDICES

A. Simulation Test Constant Temperature [100]

1. Data temperature distribution

Point	z-position (m) x 10^{-9}	Temperature (K)
0	1.643	135.95
1	1.802	136.13
2	1.940	136.19
3	2.089	135.82
4	2.237	136.03
5	2.370	136.03
6	2.514	136.11
7	2.663	136.01
8	2.822	135.73
9	3.109	135.41
10	3.505	135.49
11	3.881	135.63
12	4.257	135.73
13	5.123	135.99
14	6.480	136.01
15	7.356	136.12
16	7.732	136.46
17	8.098	136.39
18	8.494	136.83
19	8.771	135.91
20	8.920	135.88
21	9.068	136.13
22	9.216	136.06
23	9.365	136.02
24	9.504	136.06
25	9.652	136.05
26	9.801	135.89
27	9.949	136.01

B. Simulation Test Different Temperature [100]

1. Data temperature distribution

Positive Heat Flow

Point	z-position (m) x 10^{-9}	Temperature (K)
0	-4.238	105.25
1	-4.045	105.69
2	-3.831	105.88
3	-3.625	106.52
4	-3.407	108.24
5	-3.204	108.07
6	-3.204	132.45
7	-3.095	132.84
8	-2.719	133.59
9	-2.362	134.03
10	-2.005	134.72
11	-1.607	135.50
12	-1.247	136.03
13	-0.939	136.52
14	-0.313	137.45
15	0.000	138.03
16	0.311	137.12
17	0.722	136.69
18	1.105	136.00
19	1.470	135.45
20	1.835	134.86
21	2.202	134.45
22	2.580	133.57
23	2.698	133.32
24	2.698	107.96
25	2.895	108.02
26	3.114	106.52
27	3.326	106.07
28	3.543	105.89
29	3.762	105.25

Negative Heat Flow

Point	z-position (m) x 10^{-9}	Temperature (K)
0	-4.238	161.08
1	-4.045	159.98
2	-3.831	160.24
3	-3.625	159.78
4	-3.407	158.41
5	-3.204	158.51
6	-3.204	133.60
7	-3.095	132.92
8	-2.719	132.50
9	-2.362	132.13
10	-2.005	131.32
11	-1.607	130.56
12	-1.247	130.32
13	-0.940	129.3
14	-0.313	128.13
15	0.000	127.81
16	0.311	128.76
17	0.722	128.95
18	1.105	129.36
19	1.470	129.41
20	1.835	130.93
21	2.202	131.44
22	2.580	133.08
23	2.698	132.67
24	2.698	157.80
25	2.895	158.07
26	3.114	159.34
27	3.326	158.98
28	3.543	159.90
29	3.762	161.08

C. Simulation Test Heat Flux (100)

1. Data temperature distribution

Positive Heat Flow

Point	z-position (m) x 10^{-9}	Temperature (K)
0	-4.238	105.83
1	-4.045	106.19
2	-3.831	106.36
3	-3.625	106.90
4	-3.407	108.43
5	-3.204	108.07
6	-3.204	133.35
7	-3.095	133.83
8	-2.719	134.47
9	-2.362	135.11
10	-2.005	135.79
11	-1.607	136.41
12	-1.247	137.07
13	-0.939	137.90
14	-0.313	138.40
15	0.000	137.40
16	0.311	136.62
17	0.722	135.90
18	1.105	135.31
19	1.470	134.75
20	1.835	134.22
21	2.202	133.35
22	2.580	133.83
23	2.698	133.21
24	2.698	108.48
25	2.895	106.89
26	3.114	106.41
27	3.326	106.09
28	3.543	105.83
29	3.762	108.48

Negative Heat Flow

Point	z-position (m) x 10^{-9}	Temperature (K)
0	-4.238	162.08
1	-4.045	161.30
2	-3.831	161.45
3	-3.625	160.37
4	-3.407	159.17
5	-3.204	158.87
6	-3.204	135.44
7	-3.095	133.99
8	-2.719	133.64
9	-2.362	133.79
10	-2.005	132.21
11	-1.607	131.34
12	-1.247	130.65
13	-0.939	129.79
14	-0.313	129.64
15	0.000	130.68
16	0.311	130.83
17	0.722	131.56
18	1.105	131.91
19	1.470	132.79
20	1.835	133.14
21	2.202	135.44
22	2.580	133.99
23	2.698	133.32
24	2.698	158.75
25	2.895	159.70
26	3.114	160.57
27	3.326	161.05
28	3.543	161.00
29	3.762	162.08

2. Heat Flux

Positive Heat Flow

No	x-component	y-component	z-component	Total Heat Flux (MW/m^2)
1	-39.00	-101.79	-116.38	-257.17
2	-49.05	-35.83	-47.02	-131.91
3	-20.61	-13.67	-199.51	-233.79
4	-10.45	-12.44	-171.10	-193.99
5	-13.96	-29.44	-127.06	-211.06
6	-48.58	-21.52	-106.45	-235.01
7	-26.89	-23.22	-105.97	-222.23
8	-41.61	-35.56	-109.52	-202.07
9	-49.42	-37.31	-102.04	-198.16
10	23.30	51.72	98.56	189.15
11	15.97	31.00	91.01	174.33
12	10.06	23.05	97.57	189.42
13	28.84	33.39	95.81	195.05
14	31.75	21.43	104.86	223.33
15	26.70	20.84	116.82	216.28
16	15.01	9.21	174.97	199.19
17	58.32	40.74	119.77	218.84
18	25.27	39.20	119.91	184.46

Negative Heat Flow

No	x-component	y-component	z-component	Total Heat Flux (MW/m^2)
1	186.11	50.22	-55.31	181.02
2	92.40	0.04	12.38	104.81
3	170.59	-105.99	225.83	290.42
4	7.620	31.55	179.98	219.14
5	14.61	57.61	112.78	157.68
6	90.37	9.20	73.47	180.49
7	16.93	35.46	109.21	152.62
8	25.18	37.0	128.51	197.29
9	62.88	-47.73	148.92	189.80
10	-13.13	-30.40	-145.20	-195.94
11	-13.79	-5.40	-61.37	-178.46
12	-71.72	-46.40	-174.95	-252.9
13	-35.81	18.41	-196.49	-145.63
14	-123.07	-71.76	6.32	-150.45
15	-48.31	-16.54	-67.44	-146.69
16	5.33	-22.76	-187.70	-205.12
17	178.64	60.69	-431.48	-192.16
18	-312.89	125.41	-100.67	-288.14

D. Calculation of density distribution for crystal plane (100)

Molar Mass (CH_4) = $0.01604 kg/mol$

Avogadro Constant N_A = $6.023 \times 10^{23} mol^{-1}$

Convert size of layer $(\dot{A})^3$ to m^3 = $(41 \times 10^{-10}) \times (41 \times 10^{-10}) \times (118 \times 10^{-10})$

$$= 1.984 \times 10^{-25}\ m^3$$

$$Local\ Density\ (m^{-3}) = \frac{Number\ of\ molecules}{Size\ of\ layer} = \frac{2795}{1.984 \times 10^{-25} m^3}$$

$$= 1.409 \times 10^{28} m^{-3}$$

$$Density\ Distribution\ \left(\frac{kg}{m^3}\right) = Local\ Density\ (m^{-3}) \times \frac{Molar\ Mass\ (\frac{kg}{mol})}{Avogadro\ Constant\ (mol^{-1})}$$

$$= 1.409 \times 10^{28} m^{-3} \times \frac{0.01604 \frac{kg}{mol}}{6.023 \times 10^{23} mol^{-1}}$$

$$= 375.23\ kg/m^3$$